2022-06

GEOACOUSTIC INVERSION TECHNIQUES UTILIZING ACOUSTIC VECTOR SENSORS AND RESULTS FROM THE MONTEREY BAY SHELF

Geddes Lemos Guarino, Alexandre

Monterey, CA; Naval Postgraduate School

NAVAL POSTGRADUATE SCHOOL

MONTEREY, CALIFORNIA

DISSERTATION

GEOACOUSTIC INVERSION TECHNIQUES UTILIZING ACOUSTIC VECTOR SENSORS AND RESULTS FROM THE MONTEREY BAY SHELF

by

Alexandre Geddes Lemos Guarino

June 2022

Dissertation Supervisors: Kevin B. Smith
Oleg A. Godin

THIS PAGE INTENTIONALLY LEFT BLANK

REPORT DOCUMENTATION PAGE			Form Approved OMB No. 0704-0188

1. AGENCY USE ONLY *(Leave blank)*	2. REPORT DATE June 2022	3. REPORT TYPE AND DATES COVERED Dissertation

4. TITLE AND SUBTITLE GEOACOUSTIC INVERSION TECHNIQUES UTILIZING ACOUSTIC VECTOR SENSORS AND RESULTS FROM THE MONTEREY BAY SHELF	5. FUNDING NUMBERS
6. AUTHOR(S) Alexandre Geddes Lemos Guarino	
7. PERFORMING ORGANIZATION NAME(S) AND ADDRESS(ES) Naval Postgraduate School Monterey, CA 93943-5000	8. PERFORMING ORGANIZATION REPORT NUMBER
9. SPONSORING / MONITORING AGENCY NAME(S) AND ADDRESS(ES) N/A	10. SPONSORING / MONITORING AGENCY REPORT NUMBER

11. SUPPLEMENTARY NOTES The views expressed in this thesis are those of the author and do not reflect the official policy or position of the Department of Defense or the U.S. Government.

12a. DISTRIBUTION / AVAILABILITY STATEMENT Approved for public release. Distribution is unlimited.	12b. DISTRIBUTION CODE A

13. ABSTRACT (maximum 200 words)

The propagation of acoustic waves in shallow water is affected by the seabed properties. Estimating these properties in situ using acoustics is an area of research that has been in development for decades, and many techniques have been proposed using pressure-only sensors. In recent years, vector sensors have been adopted to expand the capabilities of geoacoustic inversion. This dissertation builds upon the findings of Guarino et al. reported in the *Journal of Theoretical and Computational Acoustics* and in the *Proceedings of the 24th International Congress on Acoustics,* 24–28 October 2022. It is shown that the combination of pressure and vertical velocity channels of a vector sensor can improve both the estimation of bottom attenuation coefficient, using the modal phase difference approach, and geoacoustic parameters like sound speed and density, using the multichannel average of dispersion curves. In addition, Time-warping, which is a broadly used technique for modes separation, is improved with the inclusion of a band-pass filter masking approach in the time-frequency analysis. Finally, this work suggests that waveform matching should be used as a preliminary step in dispersion curve analysis to improve inversion performance, or even be the primary choice when a vector sensor is available. The results use data collected in Monterey Bay in 2019.

14. SUBJECT TERMS geoacoustic inversion, vector sensors, time-warping. dispersion curves	15. NUMBER OF PAGES 95
	16. PRICE CODE

17. SECURITY CLASSIFICATION OF REPORT	18. SECURITY CLASSIFICATION OF THIS PAGE	19. SECURITY CLASSIFICATION OF ABSTRACT	20. LIMITATION OF ABSTRACT
Unclassified	Unclassified	Unclassified	UU

NSN 7540-01-280-5500

Standard Form 298 (Rev. 2-89)
Prescribed by ANSI Std. 239-18

THIS PAGE INTENTIONALLY LEFT BLANK

Approved for public release. Distribution is unlimited.

GEOACOUSTIC INVERSION TECHNIQUES UTILIZING ACOUSTIC VECTOR SENSORS AND RESULTS FROM THE MONTEREY BAY SHELF

Alexandre Geddes Lemos Guarino
Capitao-de-Fragata, Brazilian Navy
B.S., Universidade Federal Fluminense, 2003
M.Sc., Universidade Federal do Rio de Janeiro, 2014

Submitted in partial fulfillment of the
requirements for the degree of

DOCTOR OF PHILOSOPHY IN ENGINEERING ACOUSTICS

from the

NAVAL POSTGRADUATE SCHOOL
June 2022

Approved by:

Kevin B. Smith
Department of Physics
Dissertation Supervisor
Dissertation Chair

Oleg A. Godin
Department of Physics
Dissertation Supervisor

Roberto Cristi
Department of Electrical and Computer Engineering

Kay L. Gemba
Department of Physics

John E. Joseph
Department of Oceanography

Thomas J. Deal
Naval Undersea Warfare Center, Newport Division

Approved by:

Joseph P. Hooper
Chair, Department of Physics

Douglas J. Fouts
Chair, Department of Electrical and Computer Engineering

Michael E. Freeman
Vice Provost of Academic Affairs

THIS PAGE INTENTIONALLY LEFT BLANK

ABSTRACT

The propagation of acoustic waves in shallow water is affected by the seabed properties. Estimating these properties in situ using acoustics is an area of research that has been in development for decades, and many techniques have been proposed using pressure-only sensors. In recent years, vector sensors have been adopted to expand the capabilities of geoacoustic inversion. This dissertation builds upon the findings of Guarino et al. reported in the *Journal of Theoretical and Computational Acoustics* and in the *Proceedings of the 24th International Congress on Acoustics,* 24–28 October 2022. It is shown that the combination of pressure and vertical velocity channels of a vector sensor can improve both the estimation of bottom attenuation coefficient, using the modal phase difference approach, and geoacoustic parameters like sound speed and density, using the multichannel average of dispersion curves. In addition, Time-warping, which is a broadly used technique for modes separation, is improved with the inclusion of a band-pass filter masking approach in the time-frequency analysis. Finally, this work suggests that waveform matching should be used as a preliminary step in dispersion curve analysis to improve inversion performance, or even be the primary choice when a vector sensor is available. The results use data collected in Monterey Bay in 2019.

THIS PAGE INTENTIONALLY LEFT BLANK

TABLE OF CONTENTS

LIST OF FIGURES

THIS PAGE INTENTIONALLY LEFT BLANK

LIST OF TABLES

THIS PAGE INTENTIONALLY LEFT BLANK

LIST OF ACRONYMS AND ABBREVIATIONS

BPF	band-pass filter
CTD	conductivity, temperature, and depth
DC	dispersion curve
GA	genetic algorithm
HI	horizontally inhomogeneous
ICA	International Congress on Acoustics
JTCA	*Journal of Theoretical and Computational Acoustics*
LPF	low-pass filter
RAM	range-dependent acoustic model
RD	range dependent
SNR	signal-to-noise ratio
SSP	sound speed profile
STFT	short-time Fourier transform
TF	time-frequency
TRAD	traditional
TW	time-warping

THIS PAGE INTENTIONALLY LEFT BLANK

ACKNOWLEDGMENTS

First and foremost, I want to praise and thank God for having granted me countless blessings, knowledge, and resilience, so I was finally able to accomplish this important step in my life.

The success of this dissertation relies largely on the encouragement and guidance of many others. I take this opportunity to express my gratitude to the people who have helped me in the successful completion of this work. It would be impossible to list all names, but some of them deserve my sincere and special thanks.

First, to my wife, Ana Carolina, and my son, Mikhael, who are the greatest blessing I have in life, I want to thank you for the love and for supporting me all the time. I could not have gone this far without you. Thanks also to my parents in Brazil, Jose Luis and Albetina Maria, who always encouraged me to keep moving forward.

Second, I am grateful to the Brazilian Navy for granting me the opportunity of higher education at the Naval Postgraduate School, one of the most prestigious institutions in the world. I want to truly thank Dr. Eliane Rodriguez (Director of the Institute of Sea Studies Admiral Paulo Moreira) and Dr. Marcus Simões (Captain, Brazilian Navy, Retired) for always supporting me. I want to warmly thank Dr. Carlos Parente (Captain, Brazilian Navy, Retired, and professor in Underwater Acoustics to the *Universidade Federal do Rio de Janeiro*), a so kind and special person, for being one of my mentors in Underwater Acoustics in Brazil. I want as well to express my acknowledgment to Dr. Renato Vio (Lieutenant Commander, Brazilian Navy) for helping me when I was still in Brazil.

Third, I want to express my sincere and special gratitude to my advisors, Dr. Kevin Smith and Dr. Oleg Godin, for their extraordinary guidance and support in the development of our three papers. The uncountable meetings and hours of discussion you spent with me were crucial to the success of this research. I also want to warmly thank Dr. Kay Gemba for helping me on the last two papers.

Fourth, I want to kindly thank Dr. Michael Porter (Heat, Light, and Sound Research, Inc.) and Dr. Orlando C. Rodríguez (University of Algarve) for their

extraordinary help in my understanding of the normal mode propagation model KRAKEN, a very important tool for this research.

Last, but certainly not least, I want to thank Dr. Roberto Cristi for the several meetings we had for Signal Processing discussions, Dr. Bruce Denardo and Dr. Lawrence Ziomek for being so dedicated in teaching Acoustics, Dr. Paul Leary for guaranteeing that sea tests were done in the best way and, finally, Dr. Tsu Wei Tan for being a friend.

This work was supported by the Office of Naval Research, award No. N00014-19-WX00469, N00014-20-WX01314, and N00014-21-WX01233.

I. INTRODUCTION

In shallow water ocean waveguides, sound propagation presents a dispersive behavior. The boundaries force the creation of different modes that travel at different speeds for each distinct frequency component. Such modes are directly affected by the seabed, which makes it possible to link the modes characteristics with the bottom properties for geoacoustic inversion purposes.

Normal modes characteristics can be identified in different ways, using an array of pressure-only sensors (hydrophones) for example, or using a technique called Time-warping (TW) that has been increasingly adopted by the acoustics community. It is an elegant way of doing modes separation through non-linear resampling, based on the ideal waveguide dispersion relation. TW can be applied with only one sensor, which makes it useful in probing the properties of the acoustic field. The lack of spatial diversity provided by a single sensor is compensated by frequency diversity with the use of broadband impulsive sources, such as light bulb implosions. Details about TW can be found in the step-by-step tutorial by Bonnel *et al.* [1].

Pressure-only analysis has been extensively applied in previous TW efforts. Acoustic vector sensors, on the other hand, are a type of sensor that provides, in addition to the pressure information, three orthogonal components of particle velocity, which means it can be used for direction of arrival estimation. However, questions arise on the improvements it can provide to the geoacoustic inversion, where direction finding is not the main interest.

This work investigates the use of vector sensors in geoacoustic inversion. Two normal modes features are used: the time it takes for the modes to travel in the waveguide, which has been the most broadly used [2], [3], [4], [5], [6], and the proposed modal phase difference between pressure and vertical velocity. The analysis is done using both synthetic signals and experimental data collected on the northern shelf of Monterey Bay in 2019. For the synthetic analysis two acoustic propagation models are used—the normal mode model KRAKEN [7], and the parabolic equation model RAM [8], which were updated to also

predict components of particle velocity in addition to pressure. For the vertical velocity, the pressure gradient was calculated using a simple Fast Fourier transform-based differentiation method. For the radial velocity using RAM, the pressure gradient was calculated using the central difference approximation with a step size of $\frac{\lambda}{20}$, where the wavelength (λ) was calculated using the reference sound speed. The radial velocity was not calculated for KRAKEN. In the case of the sea test, light bulb implosions were used, and their signature recorded using a reference hydrophone. Sound speed profiles were measured with CTD casts, and data collected with a Geospectrum M20-105 vector sensor system.

The foundation for this dissertation is therefore based on a collection of three peer-reviewed articles: the first one [9] published in the *Journal of Theoretical and Computational Acoustics (*JTCA*)*, the second one [10] under review in the same Journal, and the third one [11] under review in the *Proceedings of the 24th International Congress on Acoustics (ICA2022)*.

Chapter II [9] builds upon the work done by Smith *et al.* [12] in 2007, where the concept is presented of using the vector field to invert the bottom attenuation coefficient based on the ratio of the imaginary and real parts of the acoustic radial intensity. That study emphasized the difficulties involved in the decomposition of the modal structure for practical applications. Therefore, the work presented in this chapter expands the analysis done in [12]. The concept of modal phase difference is adopted, and the analysis is done including both radial and vertical velocities. The synthetic predictions are done using the propagation models RAM and KRAKEN. The first one is updated to calculate the vector field, and the second one used to calculate the horizontal wavenumbers. Time-warping (TW) is used for modes separation, but the technique includes abrupt transitions to the processing caused by rectangular windows applied both in the time-domain, before the warping transformation, and in the time-frequency domain using binary masks, which causes distortions. This chapter proposes enhancements to the TW process, where a smoother window is included in the time-domain, and a band-pass filter (BPF) mask approach substitutes the traditional (TRAD) binary mask. In addition, the free-hand selection of modes in the time-frequency domain is substituted by a constant width mask,

which contributes to a more robust way of selecting modes. It is shown that the vertical velocity is a better option since it provides a much bigger span in phase difference compared to the radial velocity, which is easier to measure in real-world applications. The technique of estimating the bottom attenuation coefficient using the modal phase difference between pressure and vertical velocity is then tested using a Pekeris waveguide for the environmental model. The performance is evaluated using synthetic signals in two ways. First, including white noise at different signal-to-noise ratios (SNRs), and second including a real sound speed profile (SSP), which has its overall gradient scaled by a constant to evaluate the impact on the results. It is shown that although the technique is developed for a Pekeris waveguide, (1) it remains applicable in shallow-water waveguides, (2) the approach has low sensitivity to the SSP, (3) as long as normal modes are separated, the technique can be applied in range-dependent (RD) and horizontally inhomogeneous (HI) waveguides if the adiabatic approximation remains valid, and (4) a high SNR is desirable for the technique to work properly. The results make the technique a possible candidate to be used in shallow water real-world applications.

In Chapter III [10], the vector sensor is used to invert seabed properties other than the bottom attenuation coefficient presented in Chapter II. The travel time of normal modes is the main feature used, which varies over frequency for different modes. Such behavior is represented by Dispersion Curves (DCs), which are sensitive to the seabed properties and can be used for inversion purposes. The DC approach has been extensively used [13], [14], [15] applying pressure-only analysis, because it relies on fewer variables to match in the optimization process. This chapter, therefore, discusses the value added by expanding the conventional pressure-only analysis to a multichannel approach, where the average of DCs is taken considering different combinations of the vector sensor channels and results are compared with the pressure-only analysis. Synthetic signals of impulsive arrivals are modeled using KRAKEN and RAM propagation models, each being modified to predict components of the vector field. While KRAKEN is utilized to directly compute DCs, RAM provides full-field results that require the application of TW to separate the modal arrivals. Within the TW analysis, both TRAD and BPF masking methods are applied to compare stability of results. The environment modeled for the synthetic analysis and inversion

method utilize sound speed profiles measured during the Monterey Bay 2019 at-sea experiment and assume a sediment layer of constant thickness overlying a deeper sub-bottom type. White noise is added to the synthetic data at different SNRs to evaluate the impact of signal excess on the results. Inversion methods are based on genetic algorithms (GA) used to estimate the local properties of the seabed. A hybrid optimization approach is used to improve the results of the GA method. The analysis with synthetic data is consistent with the analysis of broadband, impulsive data collected from the experiment, indicating that the additional information from the vertical velocity channel further improves the geoacoustic parameter estimates.

In Chapter IV [11], vector sensor and waveform matching are used to improve the results of the DC approach. Geoacoustic inversion using DCs is very popular, but such techniques suffer from intrinsic errors associated with the separation of normal modes via TW methods which, for example, can be improved using BPF masking as shown in Chapter II. The combination of pressure and vertical velocity DCs from a vector sensor measurement also can improve results as shown in Chapter III. This chapter discusses the value added by using waveform matching as a preliminary step to improve the quality of the DC inversion method and its effect on the inversion performance. In addition, within the waveform matching approach, the estimation of bottom attenuation using the modal phase difference between pressure and vertical velocity is tested. In this analysis, the KRAKEN propagation model is used for synthetic predictions, including components of the vector field. The environment is modeled utilizing sound speed profiles measured during the Monterey Bay 2019 at-sea experiment and assumes a sediment layer overlying a deeper sub-bottom type. Inversion of experimental data is presented with a hybrid optimization approach used to improve the results and reduce uncertainty of the GA method. The results suggest that, based on the environment considered, although waveform matching can be used to improve the DC inversion, waveform matching performs better when a vector sensor is available for geoacoustic inversion.

Lastly, Chapter V presents a summary of this dissertation.

II. MODAL PHASE DIFFERENCE APPROACH

This chapter is based on the manuscript (*Bottom attenuation coefficient inversion based on the modal phase difference between pressure and vertical velocity from a single vector sensor*) that was accepted for publication in the *Journal of Theoretical and Computational Acoustics* on April 30, 2021. A version of this manuscript was published online on June 9, 2021, as [9]: A. Guarino, K. B. Smith and O. A. Godin, "Bottom attenuation coefficient inversion based on modal phase difference between pressure and vertical velocity from a single vector sensor," *J. Theor. Comput. Acoust.*, pp. 1–16, 2021, https://doi.org/10.1142/S2591728521500080.

A. INTRODUCTION

The ability to predict the sound field in shallow water relies heavily on the knowledge of the geoacoustic properties of the bottom. Estimating these properties *in situ* using acoustics has been successfully addressed through the development of four widely used techniques: matched field inversion, bottom multilayer-reflections analysis, transmission loss analysis, and modal techniques [13], [16]. The use of arrays of hydrophones, with synchronized channels to sample the field in the water column, is an important tool in such studies to achieve better estimates of mode characteristics, using this information to invert for environmental parameters. This typically involves long range tests, which provide optimal modal separation in time.

In recent years, an innovative technique that relies on an unitary transformation in the time-frequency space [17], called TW [1], has been proposed and increasingly adopted by the scientific community [14], [18], [19], [20]. This technique allows for the separation of modes within the range of a few kilometers at a single sensor in depth. The lack of spatial diversity is compensated by frequency diversity using broadband impulsive signals, which greatly reduces the cost and complexity of at-sea work and acquisition systems.

Among the approaches used for geoacoustic inversion, this chapter fits into the modal techniques. When only the pressure signal is available, the estimation of bottom properties like sound speed, density or sediment layer thickness can be accomplished by

the use of modal DCs, while the source depth or bottom attenuation can be obtained based on modal amplitudes through the use of some minimization process [13]. For example, in 2011 Bonnel and Chapman [2] used TW for mode separation based on the DC. In 2013, Zeng *et al.* [21] used a similar approach. However, in their paper, the estimated group speed is used as input to the estimation of the bottom attenuation coefficient based on the modal amplitude. In 2016, Duan *et al.* [13] showed that, although group speed modelling was very effective, the inversion of bottom attenuation coefficient from mode amplitude estimates suffers more from the interference generated during the TW mode filtering. This interference effect changes at different depths, which is why spatial diversity is applied to improve results.

Geoacoustic inversion has expanded to the use of vector sensors as well. In 2007, Smith *et al.* [12] proposed the use of modal pressure and modal radial velocity for the geoacoustic inversion of sediment attenuation coefficient. Later, Dahl and Dall'Osto [22] discussed several candidate quantities that can be measured with acoustic vector sensors and used to characterize seabed properties. In 2019, Shi *et al.* [23] provided an overview of many articles published on inversion techniques using vector sensors based on a variety of approximate or empirical methods. In 2020, Dahl and Dall'Osto [24] used a Bayesian approach where the phase difference between pressure and vertical velocity is used as input for the geoacoustic inversion of sediment layer thickness and sound speed, as well as sub-bottom sound speed.

Different from the above techniques, this chapter presents an approach based on the modal phase difference between pressure and vertical velocity to estimate the bottom attenuation coefficient. The modal signals are separated using TW and the interference between adjacent modes, which affects the phase difference processing, is mitigated by changes made to the traditional way TW is applied. The technique is based on normal modes and derived from Pekeris waveguide normal modes solutions. The results are presented for a two-homogeneous-layer environment. The impact of noise on the technique is evaluated with the addition of white noise to both pressure and vertical velocity signals before TW processing. The technique is also evaluated when the SSP is not isospeed to assess the generality of the technique, since it is based on an isospeed approach.

Finally, the horizontal wavenumbers are obtained using the propagation model KRAKEN [7]. For depth-dependent sound speed, the propagation model RAM [8] is used. Although KRAKEN can certainly be applied to depth-dependent sound speed profiles, this version of RAM was updated to provide both radial and vertical velocity components necessary to complete the analysis.

The present chapter is a simulation-based study, restricted to shallow water ($D \leq 200m$) and low-frequency impulsive sources ($f \leq 1kHz$).

B. ENHANCEMENTS TO TIME-WARPING PROCESS

The use of TW has played an important role in studies where modal filtering is necessary, especially for short to mid-range situations. Since the ocean waveguide is a dispersive environment, TW basically distorts the signal through a non-linear resampling approach to transform the input signal from a dispersive non-linear behavior into a dispersive linearized behavior, as shown in Figure 1. More details on the theory behind TW can be found in the tutorial by Bonnel *et al.* [1].

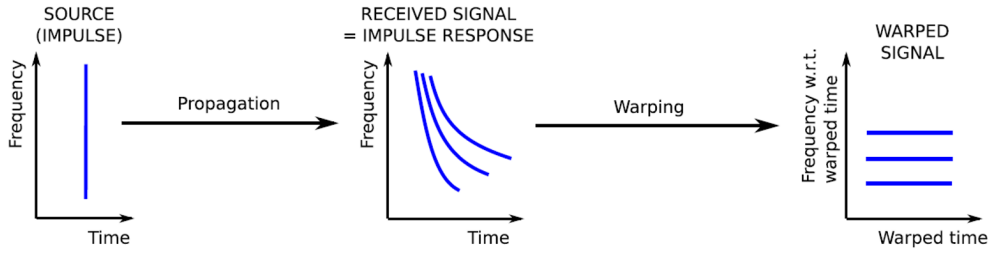

Figure 1. Time-frequency representation illustrating the dispersive behavior of an impulsive source signal after propagation and with the use of TW. Adapted from [1].

A traditional step in the TW process is the application of a binary mask in the time-frequency domain to filter out a desired mode, as depicted in Figure 2. This figure presents an idealized situation, which does not happen in practice. The first challenge arises because the most common used TW operator is based on an ideal waveguide. In non-ideal situations, the linearized modes do not appear as straight lines in the warped time domain.

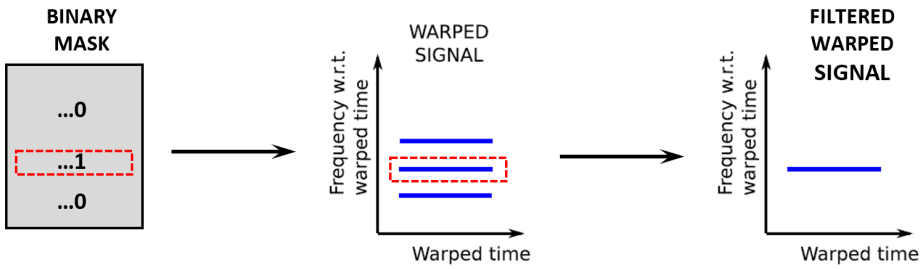

Figure 2. Idealized mode filtering approach. Adapted from [1].

The second challenge arises because it is impossible to have high resolution in both frequency and time in the time-frequency (TF) representation, which ends up resulting in some sort of leakage or interference between adjacent modes. In addition, since the TW operator is based on ideal waveguide, the distance in frequency between adjacent modes is given approximately by

$$\Delta f \approx \frac{c_w}{2H} \ , \tag{1}$$

which increases the chance of inter-modal interference, especially when the depth (H) is large. Another source of potential error is that TW depends on the ability of the operator to apply the best binary mask based on previous experience [1]. Finally, the TW inverse operator, which is given by

$$w^{-1}(t) = \sqrt{t^2 - {t_r}^2} \quad , \tag{2}$$

forces the user to cut the input signal at $t_r \leq t \leq t_r + \Delta t$, creating abrupt transitions in the signal and subsequent higher frequency components. Each of these issues can affect the input signal phase information.

All the points highlighted above are well known when using TW, and the reason why TW is best suited for estimating the DC compared to the raw mode signals themselves [1], which always suffer some form of processing distortion.

In order to address some of these issues with the goal of reducing phase sensitivity, three changes are implemented to TW processing to improve the phase difference extraction capabilities:

1. Window the input signal to smooth out abrupt transitions, as shown in Figure 3.

2. Free-hand mode selection substituted by constant vertical width selection, where the width is given approximately by Equation (1), as shown in Figure 4.

3. Substitution of the binary mask, which applies "zeros" to the unwanted frequencies and "ones" to the frequencies of interest, to a BPF with different parameters for each column of the warped-time Short Time Fourier Transform (STFT) matrix, as shown in Figure 5. Each filter has a passband equal to the region where the mask is "1."

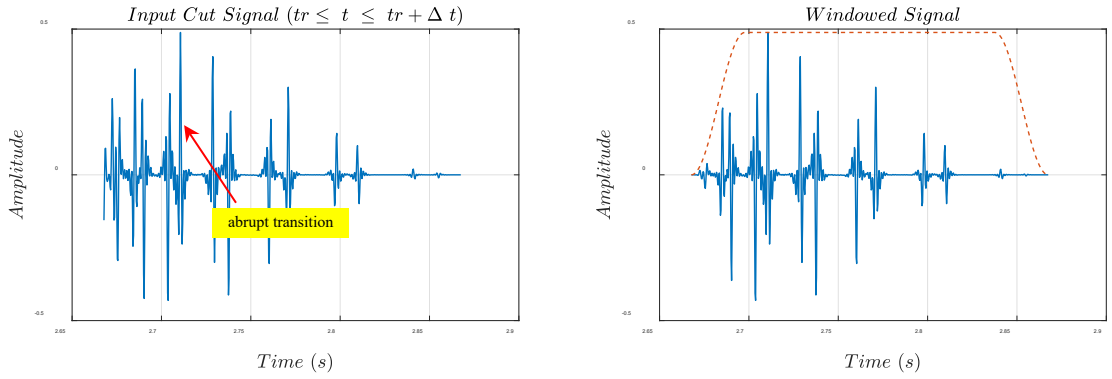

Figure 3. Example of windowed signal before warping operation.

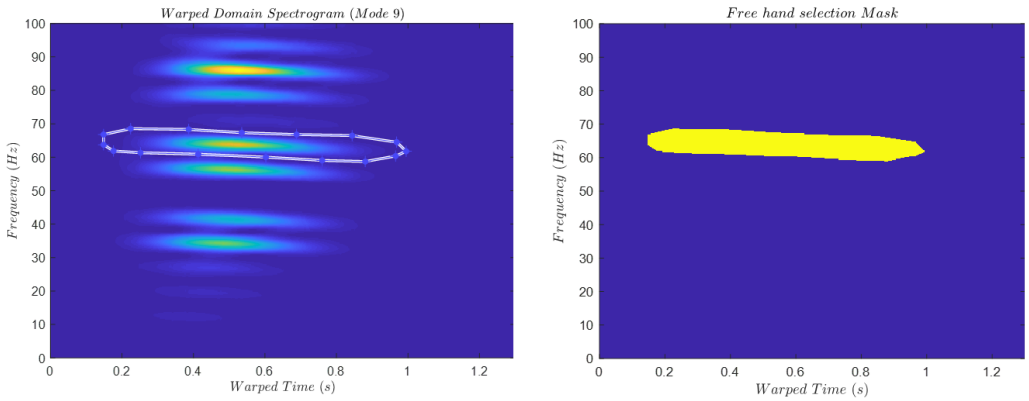

(a)

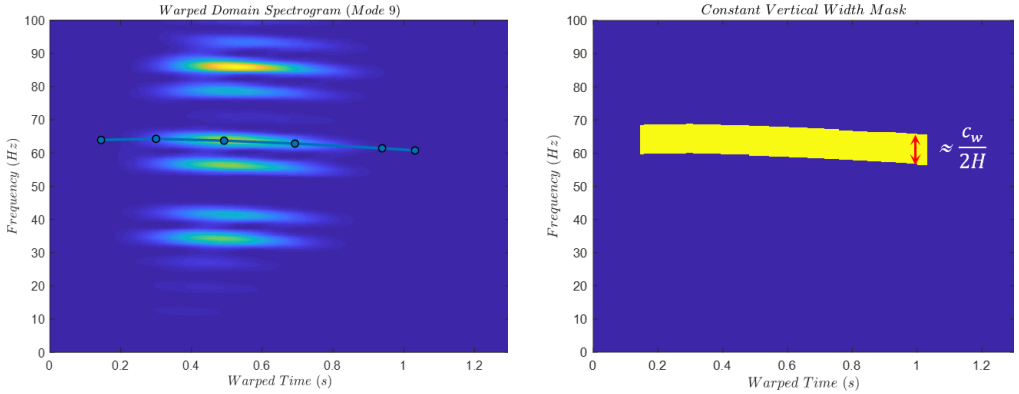

(b)

Figure 4. Free-hand selection mask (a) and selection using a constant vertical width mask (b).

The constant vertical width mask is chosen so that all filters have the same passband size. Therefore, it is only necessary to calculate the parameters of a low-pass filter (LPF) initially and then the responses of the band-pass filters are obtained from the shifting of the LPF response, that is

$$h_{BPF}[n] = A\, h_{LPF}[n]\, cos\left[2\pi \frac{f_c}{f_s}\left(n - \frac{M-1}{2}\right)\right] , \tag{3}$$

where f_c is the central frequency of each passband, M is the LPF length and A is a constant. This approach makes the calculation of the impulse response matrix faster.

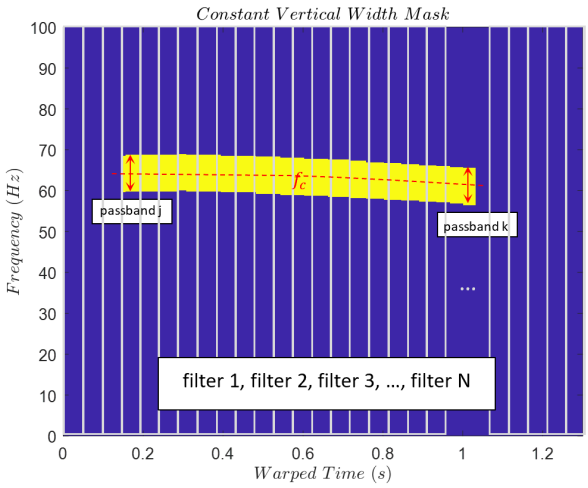

Figure 5. Each column is band-pass filtered independently.

C. PRESSURE AND VECTOR FIELD INFORMATION

The pressure field is based on the normal modes long-range solution for a Pekeris waveguide according to [12]

$$p(r,z) = j\frac{P_o}{\rho}\sqrt{\frac{2\pi}{r}}e^{-j\frac{\pi}{4}}\sum_{m=1}^{M} {A_m}^2 sin(\gamma_m z_s) sin(\gamma_m z)\frac{e^{jk_m r}}{\sqrt{k_m}}e^{-\delta_m r} \quad , \tag{4}$$

$${A_m}^2 = \left[\frac{1}{2\rho}D - \frac{1}{4\rho\gamma_m}sin(2\gamma_m D) + \frac{sin^2(\gamma_m D)}{2\rho_b g_m}\right]^{-1} \quad , \tag{5}$$

$$\gamma_m = \sqrt{k^2 - {\boldsymbol{k_m}}^2} \quad , \tag{6}$$

$$g_m = \sqrt{{\boldsymbol{k_m}}^2 - {\boldsymbol{k_b}}^2} \quad , \tag{7}$$

where the KRAKEN propagation model is used for the solution of the eigen values ($\boldsymbol{k_m}$) and the bold variables indicate complex numbers.

The radial and vertical velocities are obtained from the pressure gradient using the Euler equation

$$-\nabla p = \rho\frac{\partial u}{\partial t} \quad , \tag{8}$$

which can be found to be [12]

$$u_r(r,z) = \frac{P_o}{k\rho^2 c}\sqrt{\frac{2\pi}{r}}e^{-j\frac{\pi}{4}}\sum_{m=1}^{M}\left[-\left(\delta_m + \frac{1}{2r}\right) + jk_m\right]{A_m}^2 sin(\gamma_m z_s) sin(\gamma_m z)\frac{e^{jk_m r}}{\sqrt{k_m}}e^{-\delta_m r}, \quad (9)$$

and

$$u_z(r,z) = \frac{P_o}{k\rho^2 c}\sqrt{\frac{2\pi}{r}}e^{-j\frac{\pi}{4}}\sum_{m=1}^{M}\gamma_m\,{A_m}^2 sin(\gamma_m z_s)\,cos(\gamma_m z)\frac{e^{jk_m r}}{\sqrt{k_m}}e^{-\delta_m r} \quad . \quad (10)$$

D. PHASE DIFFERENCE PROCESSING BASED ON MODAL COMPLEX ACOUSTIC INTENSITY

The solutions for pressure, radial and vertical velocities presented in equations (4), (9), and (10) include all propagating modes. If the equations are written for just one mode, the radial and vertical velocities can be shown to be

$$u_{r_m}(r,z) = \frac{p_m}{\omega\rho}\left[k_m + j\left(\delta_m + \frac{1}{2r}\right)\right] \quad (11)$$

$$u_{z_m}(r,z) = \frac{p_m}{j\omega\rho}\frac{\gamma_m}{tan(\gamma_m z)} \quad . \quad (12)$$

Then, the average modal radial and vertical acoustic intensities can be written as

$$I_{r_m} = \frac{p_m\,{u_{r_m}}^*}{2} = \frac{|p_m|^2}{2\omega\rho}\left[k_m - j\left(\delta_m + \frac{1}{2r}\right)\right] \quad (13)$$

$$I_{z_m} = \frac{p_m\,{u_{z_m}}^*}{2} = j\frac{|p_m|^2}{2\omega\rho}\frac{{\gamma_m}^*}{tan(\gamma_m z)^*} \quad . \quad (14)$$

The modal intensities can also be represented as

$$I_{r_m} = \frac{|p_m|\left|u_{r_m}\right|e^{j\Delta\theta_{(r)}}}{2} \quad (15)$$

$$I_{z_m} = \frac{|p_m|\left|u_{z_m}\right|e^{j\Delta\theta_{(z)}}}{2} \quad . \quad (16)$$

The radial phase difference is related to the modal radial intensity by

$$tan\left[\Delta\theta_{(r)}\right] = -\frac{\delta_m + \frac{1}{2r}}{k_m} \quad . \quad (17)$$

Considering that for TW the range must be of some kilometers for the technique to work well, the phase difference between pressure and radial velocity can be approximated to

$$\Delta\theta_{(r)} \approx -\frac{\delta_m}{k_m} \quad . \tag{18}$$

In the same way, the phase difference between pressure and vertical velocity can be obtained from

$$\Delta\theta_{(z)} = \frac{\pi}{2} + arctan\left(\frac{Im\left\{\frac{{\gamma_m}^*}{tan(\gamma_m z)^*}\right\}}{Re\left\{\frac{{\gamma_m}^*}{tan(\gamma_m z)^*}\right\}}\right) \quad , \tag{19}$$

where "Im{}" and "Re{}" are the imaginary and real parts of a complex number. Since δ_m is small, Equation (19) can be Taylor expanded with a linear approximation around $\delta_m = 0$, as

$$\Delta\theta_{(z)} \approx \frac{\pi}{2} + \frac{\partial}{\partial\delta_m}\left(\frac{Im\left\{\frac{{\gamma_m}^*}{tan(\gamma_m z)^*}\right\}}{Re\left\{\frac{{\gamma_m}^*}{tan(\gamma_m z)^*}\right\}}\right)\Bigg|_{\delta_m=0} \delta_m \quad . \tag{20}$$

Since $\boldsymbol{k_m} = k_m + j\delta_m$ and $\delta_m \ll k_m$, Equation (6) can be approximated to

$$\gamma_m = \sqrt{k^2 - {k_m}^2}\left[1 - j\frac{k_m\delta_m}{k^2 - {k_m}^2}\right] . \tag{21}$$

Therefore, it can be shown that Equation (20) can be approximated as

$$\Delta\theta_{(z)} \approx \frac{\pi}{2} + \frac{k_m}{k^2 - {k_m}^2}\frac{sinc\left(\frac{2}{\pi}\sqrt{k^2 - {k_m}^2}\, z\right) - 1}{sinc\left(\frac{2}{\pi}\sqrt{k^2 - {k_m}^2}\, z\right)}\,\delta_m \quad , \tag{22}$$

where $sinc(x) = \frac{sin\,(\pi x)}{\pi x}$.

In theory, the modal attenuation coefficient can be obtained with the use of either Equation (18) or Equation (22). Next, with the use of perturbation analysis for the modal attenuation parameters, the bottom attenuation coefficient can be inverted based on the following expression [12], which relates the modal attenuation coefficient with the bottom attenuation coefficient,

$$\alpha_b = \frac{2\, k_m\, \rho_b c_b\, g_m}{A_m^2\, sin^2\left(\gamma_m D\right)\omega}\delta_m \quad . \tag{23}$$

To compare which phase difference, radial or vertical, produces the biggest angle variation, Equation (22) can be written as

$$\Delta\theta_{(z)} \approx \frac{\pi}{2} + A\,\frac{\delta_m}{k_m} \quad , \tag{24}$$

$$A = \frac{\alpha^2}{1-\alpha^2}\,\frac{sinc\left(\frac{4f}{c}\sqrt{1-\alpha^2}\,z\right) - 1}{sinc\left(\frac{4f}{c}\sqrt{1-\alpha^2}\,z\right)} \quad , \tag{25}$$

and

$$k_m = \alpha k \quad . \tag{26}$$

Combining equations (18) and (24), we obtain

$$\Delta\theta_{(z)} \approx \frac{\pi}{2} - A\Delta\theta_{(r)} \quad , \tag{27}$$

$$A \approx -\frac{d\Delta\theta_{(z)}}{d\Delta\theta_{(r)}} \quad . \tag{28}$$

Figure 6 illustrates some results for $log_{10}(|A|)$ if we consider the trapped modes with $\alpha \leq cos(20^o)$.

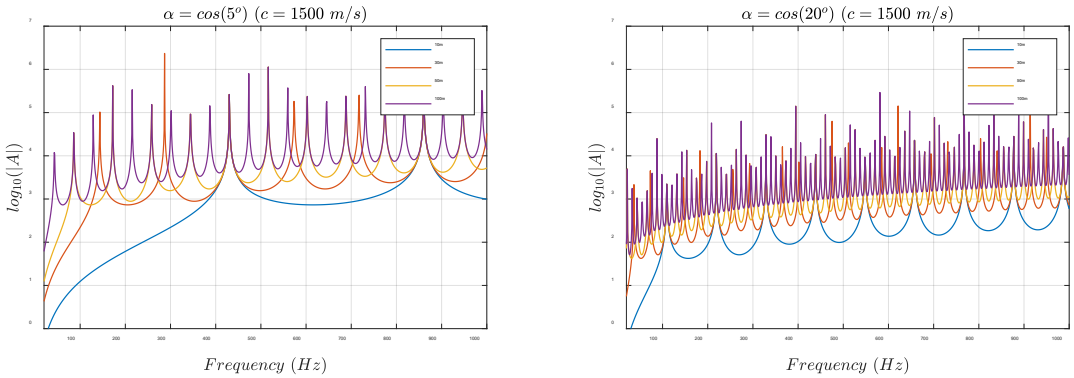

Figure 6. Factor "A" behavior for "α" equals cos(5º) and cos(20º).

As shown in Figure 6, the vertical velocity produces a much bigger span in phase difference compared to the radial velocity, which tends to make it easier to measure it in real world applications. For example, when $\alpha = cos(20^o)$, above 400 Hz the vertical velocity produces a span in phase difference at least 100 times larger than the one produced by the radial velocity. In addition, the phase difference using radial velocity is so small making it more susceptible to signal processing artifacts. This chapter, therefore, is based on the vertical velocity use, even though the vertical channel tends to be noisier due to a bigger coupling with the surface noise.

Figure 7 presents the overall processing proposed in this chapter, based on the phase difference between modal pressure and modal vertical velocity, for the inversion of the bottom attenuation coefficient.

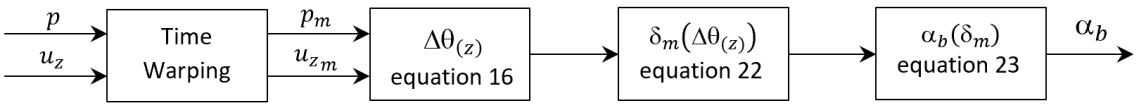

Figure 7. Procedure to invert the bottom attenuation coefficient.

E. RESULTS

We shall now consider results computed in a two-layer homogeneous waveguide, as depicted in Figure 8. The water column is 100 m deep with sound speed $c(z)$. The bottom is treated as a fluid with sound speed 1600 m/s, density of 1.2 g/cm^3 and attenuation coefficient of 0.4 dB/m/kHz.

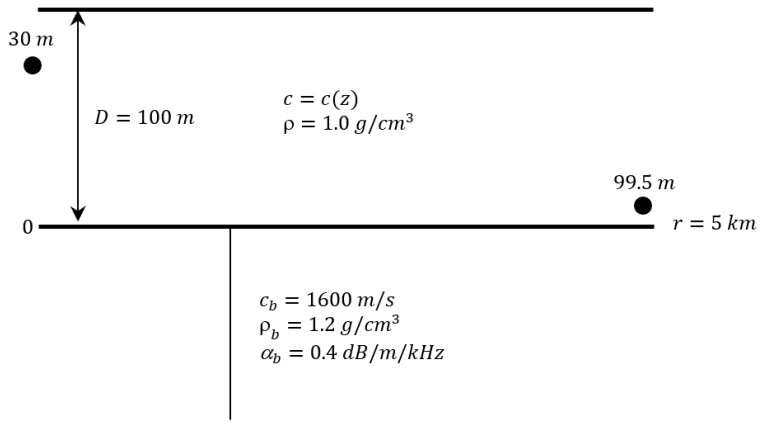

Figure 8. Schematic representation of the waveguide properties used in calculations.

An impulsive broadband signal source ranging from 20 to 1000 Hz is placed at 30 m depth and a vector sensor is placed at 99.5 m depth at a range of 5 km. The source signature is windowed using a Tukey 0.5 window, as shown in Figure 9.

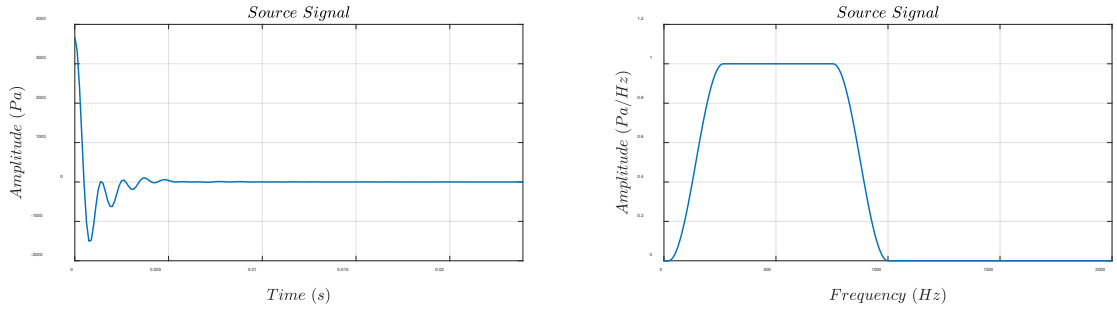

Figure 9. Source signature.

The sound speed profiles to be considered are based on a real SSP ($c[n]$) with overall gradient scaled by the constant β, according to

$$c[n]_{new} = 1500 + \beta(c[n] - c[end]) \quad . \tag{29}$$

The resulting SSP are shown in Figure 10, where $0 \leq \beta \leq 2$.

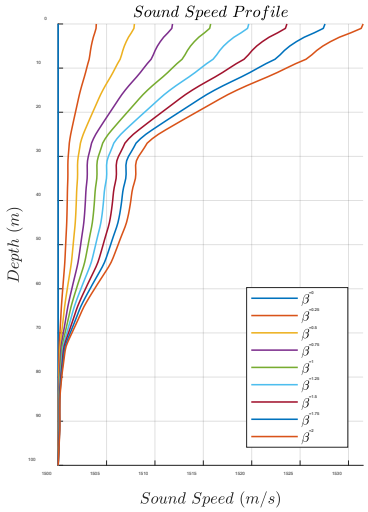

Figure 10. Sound speed profiles for various factors of b.

Figure 11 illustrates the pressure and vertical velocity signals received at 99.5 m in this environment, while Figure 12 shows the spectrogram of the pressure and vertical velocity signals after warping.

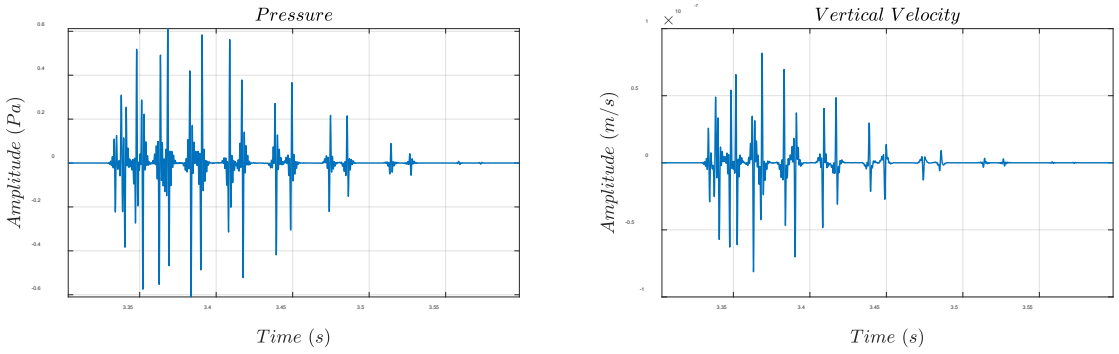

Figure 11. Theoretical pressure and vertical velocity signals at the vector sensor.

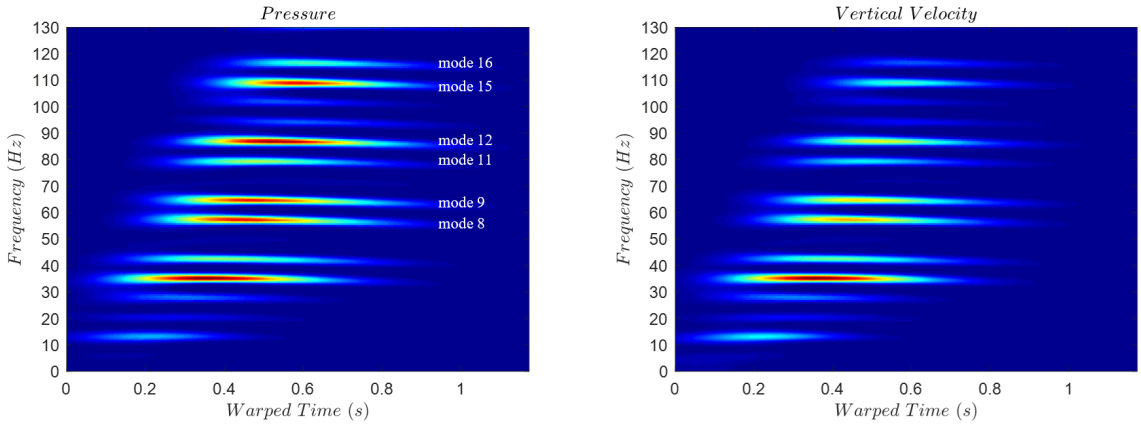

Figure 12. Pressure and vertical velocity spectrograms after warping.

Next, pressure and vertical velocity of modes 8, 9, 11, 12, 15, and 16 are filtered. Figure 13 illustrates mode 12 results obtained from (a) phase difference and (b) modal attenuation coefficient.

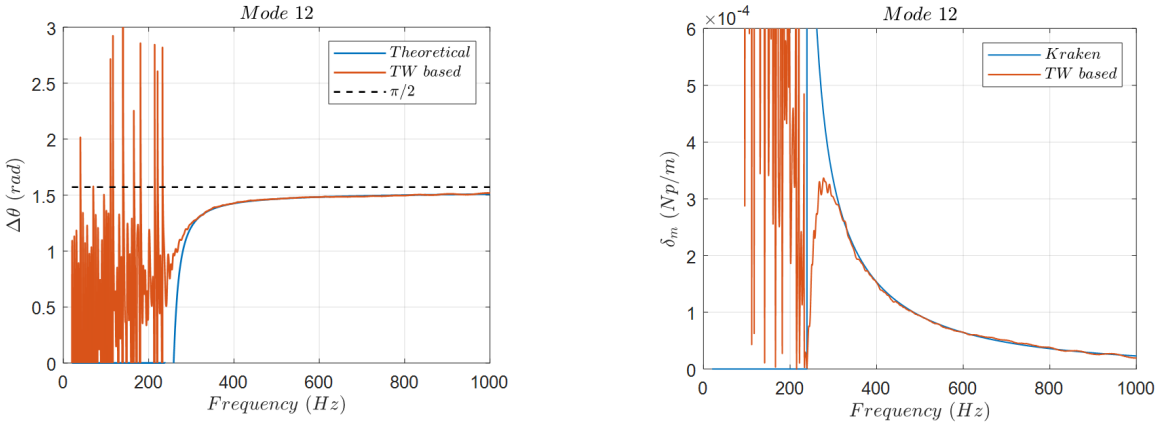

(a) (b)

Figure 13. Comparison between theoretical and TW: phase difference (a) and modal attenuation coefficient (b).

Finally, Figure 14 illustrates the estimated bottom attenuation coefficient for the six modes in two ways: original result (a) and shifted and aligned with the first mode position (b).

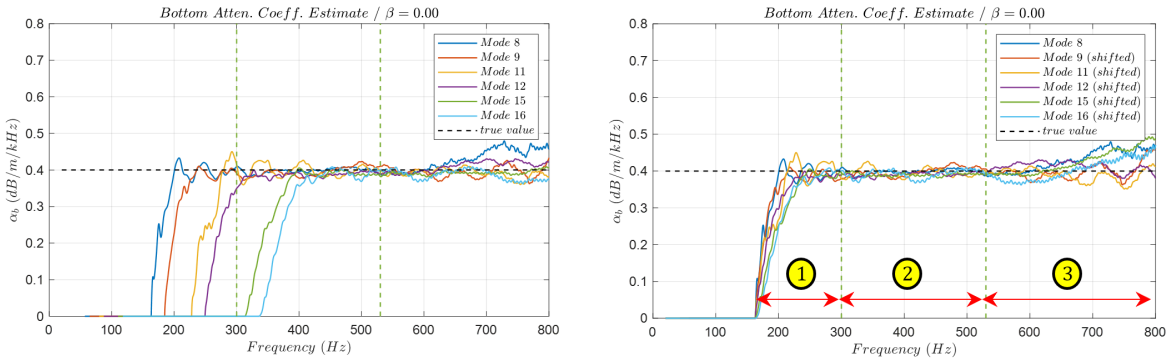

(a) (b)

Figure 14. Bottom attenuation coefficient estimate for modes 8,9,11,12,15,16: original position (a) shifted and aligned with the first mode position (b).

When the mode results are shifted and aligned with the first mode, it is possible to identify in Figure 14(b) the formation of three regions of similar characteristics. For the purpose of bottom attenuation coefficient estimate, region 2 is chosen since it is more stable. Figure 15(a) illustrates the mode results average curve according to Figure 14(b) with the bottom attenuation coefficient being estimated based on the mean value between 300 and 530 Hz equal to 0.394 dB/m/kHz with a true value of 0.4 dB/m/kHz. Following an analogous procedure, Figure 15(b) illustrates the results if white noise is included to Figure 11 (i.e., before TW). For the results shown in Figure 15(b), region 2 is not fixed. Instead, its size and position vary and it is chosen to take advantage of the most stable frequency range for each SNR value. It is worth noting that, in order to produce stable results, this analysis suggests loud signals with SNR > 20 dB may be required. Such SNR values are achievable with the use of explosive (e.g., SUS) or implosive (e.g., light bulbs) sources.

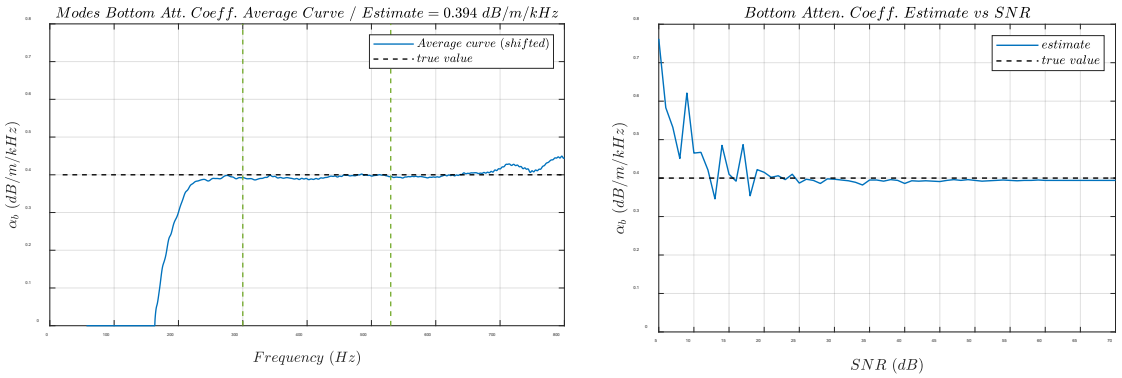

(a) (b)

Figure 15. Bottom attenuation coefficient estimate: without noise (a) and in the presence of white noise (b).

All results presented so far have considered β = 0, that is the horizontal wavenumbers $k_m(f)$ obtained from KRAKEN refer to a Pekeris isospeed channel. Keeping the same horizontal wavenumbers $k_m(f)$, the results in Figure 16 show the sensitivity of the technique to depth-varying sound speed profile environments. As can be noted, the method is not highly sensitive to the sound speed gradient.

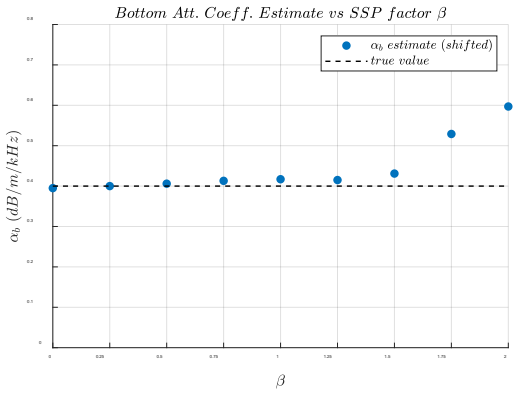

Figure 16. Bottom attenuation coefficient vs. SSP factor "b."

F. DISCUSSION

The modal vertical phase difference method presented in this chapter proposes a technique that relies only on one sensor. Since the bottom attenuation coefficient

information is embedded in the phase difference between modal pressure and modal vertical velocity, one of the key factors of the technique is the mode separation. TW is used to separate the modes. However, it suffers from modal interference when filtering the modes in the time-frequency domain. The enhancements in TW help to provide smoother results compared to the traditional way TW is generally applied. Figure 17 compares the results in a noiseless situation and isospeed channel for (a) improved TW processing and (b) traditional TW processing.

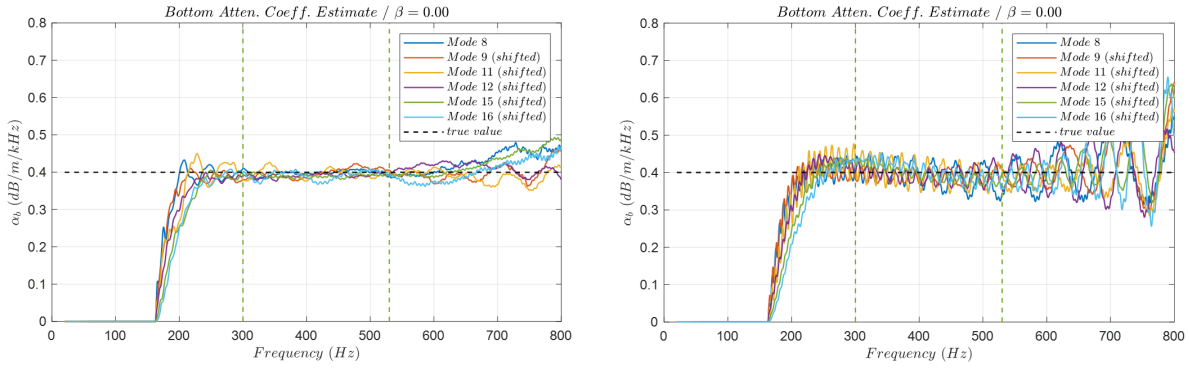

(a) (b)

Figure 17. Comparison between improved TW processing (a) and traditional TW processing (b).

The modal phase difference method has been developed for a Pekeris waveguide. However, the technique remains applicable in shallow-water waveguides with depth-dependent sound speed in water and is robust with respect to uncertainty in the knowledge of the sound speed profile. Figure 16 illustrates the effect of unknown negative sound-speed gradients in the water column on the bottom attenuation estimate, when only near-bottom sound speed is known. The steeper the sound speed gradient, the more energy is pushed towards the bottom, which is expected to increase the attenuation perceived at the near-bottom receiver. As expected, the retrieved value of the bottom attenuation increases with increasing parameter β in Equation (29) (see Figure 16). However, even for β=1.25, which means an overall gradient of approximately $\Delta c = 20\ m/s$ in $\Delta z = 100\ m$, the bottom attenuation coefficient presents only a small error of 3.75%. Thus, in the example

considered, the sound speed uncertainty as large as 20 m/s has only marginal effect on the retrieval of the bottom attenuation by the proposed technique.

The input data for the bottom attenuation retrieval are the phase shifts between the acoustic pressure and vertical component of particle velocity in individual normal modes. The phase shift is independent of the mode amplitude and is determined by respective modal shape functions. The technique has been introduced above for range-independent (RI) waveguides. However, as long as normal modes are separated, the technique can be applied without modifications in range-dependent (RD) and horizontally inhomogeneous (HI) waveguides as long as the adiabatic approximation [25] remains valid in these waveguides. In this approximation, energy exchange between normal modes is negligible, and the acoustic field consists of modes with the same local shape functions as in the corresponding RI waveguide. With the input data related to the shape functions of local modes rather than the travel time of adiabatic modes, the technique proposed in this chapter does not suffer from the limitations of TW-based geoacoustic inversions in RD and HI waveguides [15]. In RD and HI waveguides, the bottom attenuation measured with the proposed technique has the meaning of the attenuation at the receiver site and not the path-averaged bottom attenuation.

G. CONCLUSION

This chapter presented a phase difference inversion scheme using TW applied to the pressure and vertical velocity channels of a vector sensor for the estimation of the bottom attenuation coefficient. Despite some limitations of TW, the new approach was able to improve the phase difference results and consequently estimated the bottom attenuation coefficient in a smoother way. A high SNR is desirable for the technique to work properly, which is not a strong restriction when impulsive sources are used. In addition, it was demonstrated that the approach has low sensitivity to the sound speed profile, which makes it a possible candidate to be used in shallow water real world applications.

III. MULTICHANNEL DISPERSION CURVE INVERSION

This chapter is based on the manuscript [10] (*Geoacoustic inversion with a single vector sensor and multichannel dispersion*) that was submitted for publication in the *Journal of Theoretical and Computational Acoustics* on March 6, 2022. The manuscript is under review with the number JTCA-D-22-00004.

A. INTRODUCTION

In shallow water the seabed properties influence how the propagation of acoustic waves takes place in the underwater acoustic waveguide. The travel time of different mode components is one of the features affected by the bottom characteristics, which leads to its use in ocean remote sensing for the geoacoustic inversion of environmental parameters. Propagation in confined environments presents a dispersive behavior, that is the boundaries force the creation of different modes that travel at different speeds for each distinct frequency component in a certain frequency range. Consequently, a different set of modal DCs can be linked directly to a set of bottom parameters.

The most broadly used feature of propagating normal modes is the modal group speed dispersion [2], [3], [4], [5], [6]. Different approaches have been used to identify normal modes properties. For instance, in 2007 LI Zheng-Lin *et al.* [4] used a fiber-optic hydrophone horizontal array whereas in 2019 Tan *et al.* [20] applied noise interferometry to estimate an empirical Green's function, allowing for mode separation with the use of TW.

TW has been increasingly adopted by the acoustics community over the years. It is an elegant way for resolving modes with only one sensor. The spatial diversity provided by an array of sensors can be replaced by only one sensor when broadband impulsive signals provide frequency diversity to allow for the geoacoustic inversion task. Bonnel *et al.* present more details about TW in [1].

Many researchers have retrieved DCs using TW. For example, in 2016, Duan *et al.* [26] applied a sequential inversion approach, using DC estimates to invert for bottom sound speed and density and sediment thickness. They still showed that better DCs estimates can

be obtained using source deconvolution when light bulb implosion is applied. In 2018, Bonnel *et al.* [14] included high order modes DCs to the inversion problem and, in 2019, Godin *et al.* [15] showed that sea floor slopes contribute to the success of mode filtering using TW, making the DCs more similar to the DCs in an ideal waveguide.

When it comes to vector sensors, such devices provide more information; that is, besides pressure signal, three orthogonal components of particle velocity are available. Apart from its application in direction finding or target tracking, it also is useful for geoacoustic inversion. For example, in 2010 Santos *et al.* [27] used a four-element vector sensor array to estimate seabed properties based on matched-field inversion. In 2012, Rodríguez *et al.* [28] presented results on geoacoustic estimation using vector sensor based on pressure gradients, and in 2016 Dall'Osto *et al.* [29] demonstrated the effect of multipath interference on the degree of circularity when two components of particle velocity are not in phase and its application in geoacoustic inversion.

This chapter investigates the hypothesis that the combination of DCs can improve results over pressure-only analysis, which in this work is tested by averaging multichannel DCs. In theory, there should be no difference in the DCs obtained using either pressure or velocity signals. However, the velocity channels of a vector sensor are not equally sensitive to high and low order modes [3]. As a result, it is common to observe vector sensor velocity signals with different signal-to-noise ratios. To show this, we analyze synthetic data as well as impulsive acoustic data collected on a single vector sensor deployed on the northern shelf during the Monterey Bay 2019 experiment. The work is restricted to shallow water ($D \leq 200m$) and low-frequency impulsive sources ($f \leq 1\ kHz$).

First, synthetic signals are used to calibrate processing techniques. Normal mode model KRAKEN [7] and Parabolic equation model RAM [8] are used, each being modified to predict particle velocity components. KRAKEN is utilized to directly compute DCs using the adiabatic approximation. Its individual mode components waveforms are used to evaluate the technique's capabilities without the influence of TW. In comparison, RAM outputs the full-field, which requires TW to separate the modal arrivals. Additionally, white noise is added to the synthetic data at different signal-to-noise ratios to evaluate the impact

of signal excess on the results. Within the TW analysis, both binary masking and band-pass filter masking [9] methods are applied to compare stability of results.

Some sources of error are known to affect the DC inversion method, such as the process of retrieving DC from a time-domain signal. Reassigned spectrograms rely on time-frequency (TF) analysis and suffer from the lack of high resolution in both time and frequency representation, causing interference in the TF domain and distortions to the retrieved DC. Another source of error is due to TW. Although TW itself uses a warping operator that possesses a one-to-one correspondence between all points in the warped and unwarped domains [1], TW uses a not-perfect warping operator based on ideal waveguide, which affects its performance in more complex situations. In addition, time-frequency mode extraction using binary mask adds up to the causes of retrieved DC distortions [9]. In such cases, it is expected that DC multichannel averaging may help to mitigate such problems.

The environment modeled for the synthetic analysis and inversion method utilizes sound speed profiles measured during the test event and assumes a sediment layer of constant thickness overlying a deeper sub-bottom type. Genetic algorithms (GAs) can rapidly locate the global optimum; however, it can be slow to locate the exact local optimum in the region of convergence. A hybrid optimization approach is implemented to expedite convergence.

This chapter is organized as follows: the sea test characteristics and environment model are presented, the inversion scheme is defined and tested, and the hybrid optimization approach is evaluated. Next, the preliminary synthetic signals analysis results are shown, which suggests that modest improvements in geoacoustic inversion results may be obtained by combining the vertical velocity channel of the vector sensor with the pressure channel. The manuscript concludes with our analysis of experimental data followed by a discussion of results.

B. SEA TEST CHARACTERISTICS AND ENVIRONMENTAL MODEL

The acoustic data was collected in 2019 in Monterey Bay. Figure18(a) shows a bathymetric map of the experiment location. The location of two yellow markers labeled

Shot 3 and Shot 4 correspond to two light bulb [Figure18(b)] implosions. These implosions are executed using a metal sabot that travels along the rope and hits the activation mechanism, breaking the light bulb. This type of acoustic source is simple yet robust and provides low-frequency impulsive signals [30] used for analysis in this work. The environmental model assumes a sediment layer of constant thickness overlying a deeper sub-bottom type, as illustrated in Figure18(c).

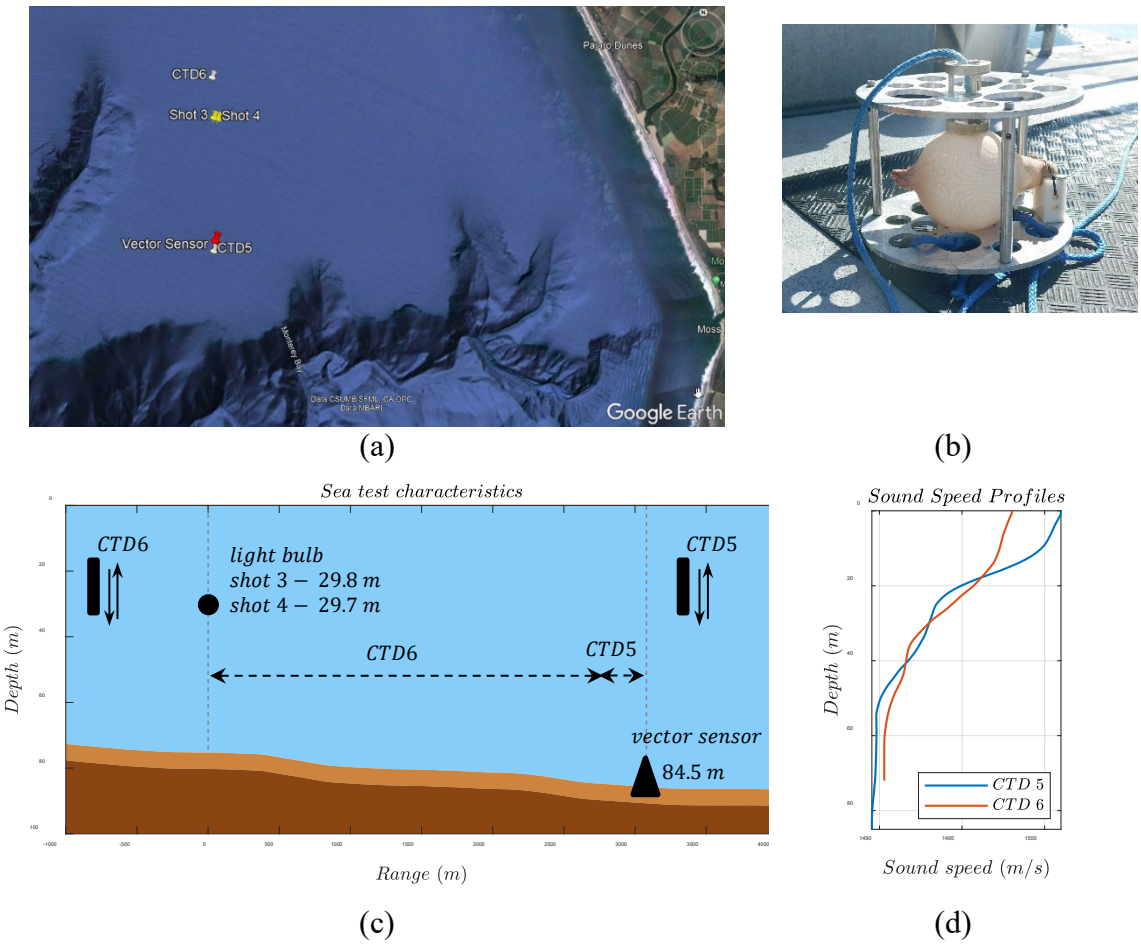

Figure 18. Overall sea test characteristics. Location of the test event in Monterey Bay, showing the positions of the two light bulb implosions in yellow, CTD castings in white and vector sensor in red (a). Light bulb system setup. The implosion is carried out sending a messenger from the boat that travels along the rope and breaks the light bulb (b). Range dependent environmental model used in the analysis (c). Sound speed profiles (SSPs) measured during the sea test (d).

Prior information from two CTD casts are used in this work [Figure18(d)]: CTD6 and CTD5 are taken at the vicinity of the source (light bulb) and receiver (vector sensor), as shown in Figure18(c). The range dependent transition from CTD6 to CTD5 water-column sound speed profiles is estimated using waveform matching optimization, where CTD6 covers ~90% of the range between the light bulb position and the vector sensor position. The remaining 10% is covered by the SSP calculated from CTD5 [see horizontal line with arrows at ~50m depth in Figure18(c)].

A reference hydrophone near the source recorded the time-domain waveform of the implosion Shots 3 and 4. This allowed us to estimate the source depth with a short-range vertical propagation model. Figure 19 shows the signals measured on the reference hydrophone (red trace) compared to the synthetic results (blue trace). The direct path occurs at about 0.01s, the surface reflection at about 0.05s for both shots. The good agreement between data and model provides a source depth estimate for Shots 3 and 4 of 29.8 and 29.7 m, respectively. Shot 3 depth is selected to the preliminary synthetic signal analysis.

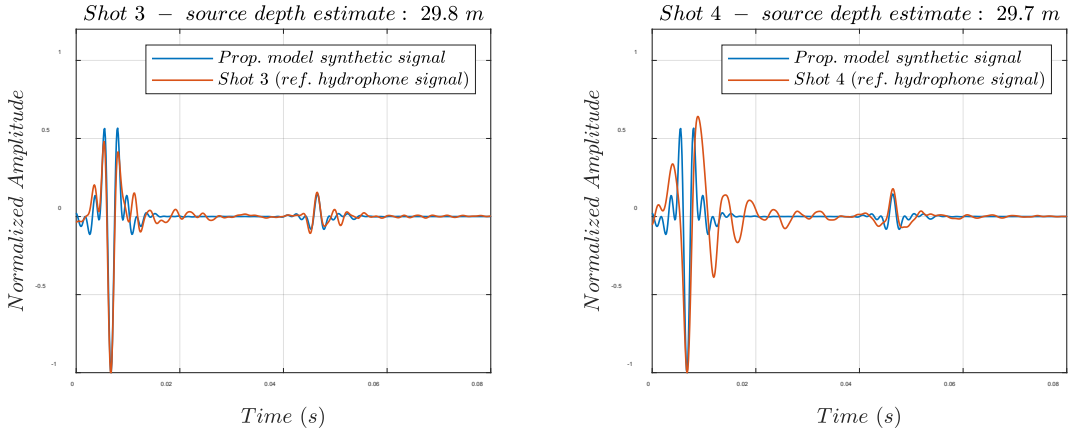

(a) (b)

Figure 19. Source depth estimates using a short-range vertical propagation model and data from the reference hydrophone. Shot 3 source depth is 29.8 m (a) and Shot 4 source depth is 29.7 m (b).

A Geospectrum M20-105 vector sensor system was used in the sea test. The sensor itself was suspended from the frame with a nylon rope as shown in Figure 20(a). The system frame was place on the seafloor at ~85 m depth [Figure 18(c)]. To mitigate flow noise, the system was covered prior to the deployment with a fabric as shown in Figure 20(b).

(a) (b)

Figure 20. Vector sensor system used in the sea test, model GTI M20-105 (a) and the system was covered to minimize flow noise (b).

As for the effective bottom model [3], in the preliminary synthetic signal analysis both sediment layer and sub-bottom have constant sound speed and density. The sea test data analysis includes a constant sound speed gradient to the sediment layer.

Regarding ground truth information [3], the bottom is composed mainly by mud, very fine sand, and silt according to the California Seafloor Mapping Program [31].

C. RESULTS

1. Inversion Method

The inversion method uses DC replicas directly computed by KRAKEN group speed. Since bathymetry has a slow variation, adiabatic approximation is applied according to [32].

$$p(r,z) \approx \frac{j}{\rho(z_s)\sqrt{8\pi r}}\ e^{-j\frac{\pi}{4}} \sum_{m=1}^{\infty} \psi_m(0,z_s)\,\psi_m(r,z) \frac{e^{j\int_0^r k_m(r')dr'}}{\sqrt{k_m(r)}}. \tag{30}$$

Since KRAKEN is a normal modes model, the total range is divided into N range segments and it can be shown that the equivalent group speed is given by

$$c_{gm_e} = \frac{N}{\sum_{i=1}^{N} \frac{1}{c_{gm_i}}}. \tag{31}$$

N is determined based on the constraint that the maximum bathymetry vertical step must be less than or equal to the highest frequency component wavelength. Figure 21 shows a comparison between KRAKEN and RAM when such constraint is applied to the environment model shown in Figure18(c), using the geoacoustic parameters shown in the column "TRUE value" of Table 1 and frequency range 80 to 420 Hz. Once the correct number of range segments has been determined, the DCs are easily obtained using Equation 31 and KRAKEN group speed results.

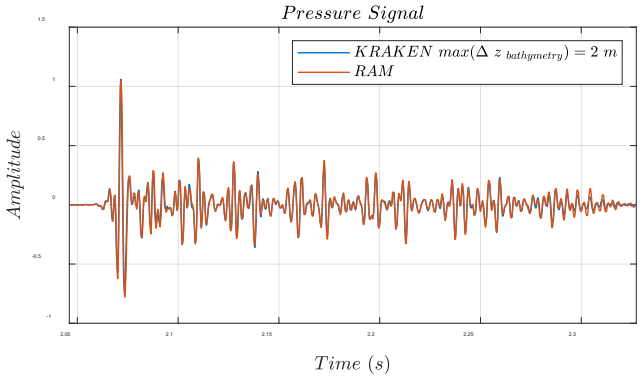

Figure 21. Comparison between RAM and KRAKEN using a bathymetry maximum vertical step of 2 m and 11 range segments, which shows that the number of range segments is adequate, providing good matching between both propagation models full-field predictions.

Concerning the optimization part, GA is used. It is a population-based search and optimization method that mimics the process of natural evolution. However, a finite population size influences its sampling ability, which affects performance [33]. In view of

GA convergence issues, and considering the time to run the increased number of optimizations due to the multichannel technique used in this work, a hybrid approach is adopted with two GA instances followed by two Bayesian optimization instances, where the lower and upper bounds of each searched parameter shrink accordingly as the optimization process moves forward. The optimization tools are based on MATLAB function "ga" within the Global Optimization Toolbox and on the function "bayesopt" within the Statistics and Machine Learning Toolbox.

The cost function d is based on the minimization of the mean squared error average between the DC estimate, which is calculated from data, and DC replica travel times with frequency being the independent variable according

$$d = \frac{1}{M}\sum_{m=1}^{M}\frac{1}{N_m}\sum_{i=1}^{N_m}\left[\hat{t}_m(f_i) - t_{m_r}(f_i) + dt\right]^2 , \tag{32}$$

where M is the number of modes, N_m is the number of points of a specific mode DC, $\hat{t}_m$ is the DC estimate travel time, t_{m_r} is the DC replica travel time and dt is a time shift included as a search parameter when the sea test signals are used to compensate for small range mismatches.

The performance evaluation of the optimization approach was conducted as follows: the same geoacoustic parameters shown in the column "TRUE value" of Table 1 were picked to generate DC using KRAKEN group speed. In all trials tested, the hybrid optimization found the exact vector indicating a stable performance. Table 1 illustrates one trial and the vectors found by each optimization round, where it is possible to see the continuous improvement in geoacoustic parameters estimation as the optimization moves to the next round.

Table 1. Optimization performance test, where it is shown the continuous improvement in the geoacoustic parameters estimation as the optimization moves to next round.

Parameter	Unit	Search bounds	Step	TRUE value	GA round 1 estimate	GA round 2 estimate	Bayesian round 1 estimate	Bayesian round 2 estimate
c_s	m/s	1440 - 1600	1	**1480**	1473	1480	1480	**1480**
ρ_s	g/cm^3	1.20 - 1.60	0.01	**1.40**	1.39	1.42	1.39	**1.40**
H_s	m	1.0 – 20.0	0.1	**10.0**	10.5	10.0	10.0	**10.0**
c_b	m/s	1600 - 2000	1	**1700**	1712	1701	1700	**1700**
ρ_b	g/cm^3	1.60 - 2.40	0.01	**1.80**	1.93	1.89	1.79	**1.80**

c_s is the sediment sound speed (m/s), ρ_s the sediment density (g/cm^3), H_s the sediment thickness (m), c_b the sub-bottom sound speed (m/s), and ρ_b the sub-bottom density (g/cm^3).

2. Preliminary Evaluation Using Synthetic Signals

The evaluation using synthetic signals aims to demonstrate if the vector-sensor multichannel DC averaging can improve results over pressure-only analysis. White noise is added with the same ratio to the pressure and velocity full-field predictions at the following SNRs: ∞, 25, 20, 15 and 10 dB. Regarding modes separation, two approaches are tested: in the first one, KRAKEN provides the individual modes waveforms already separated in order to test the results without the influence of TW. In the second one, RAM provides full-field results that require the application of TW to separate the modal arrivals. TW is then tested using binary masking and BPF masking methods to compare stability of results.

The overall evaluation is realized with and without DC averaging, which can include six different calculations: pressure-only, radial velocity-only, vertical velocity-only, combination of pressure and radial velocity, combination of pressure and vertical velocity and finally, combination of pressure, radial and vertical velocities. When KRAKEN individual modes waveforms are used, the number of calculations is reduced to three, since radial velocity is not available. The environment model used is shown in Figure18(c), source depth of 29.8 m, the range is 3080 m and the frequency band 80–420 Hz.

Figure 22 shows the DCs obtained using KRAKEN individual mode waveforms applying reassigned spectrogram and ridge function, and including modes 5, 7, 8, 9, 10 and 11. Such modes were picked to minimize DC distortions caused by source or receiver being close to mode function nodes, what tends to happen with the vertical velocity since the receiver depth is close to the bottom.

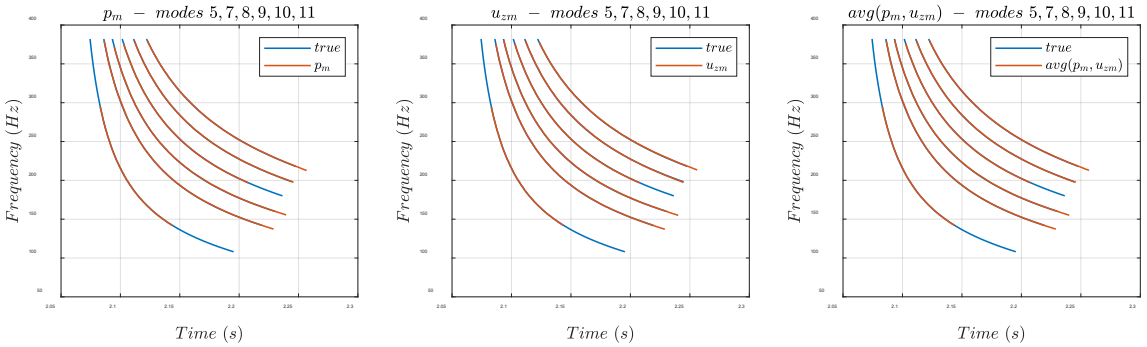

(a) (b) (c)

Figure 22. DCs obtained applying reassigned spectrogram and ridge function to KRAKEN individual mode waveforms. The "true" DC is provided by KRAKEN group speed using adiabatic approximation. Comparison between pressure DC and true DC (a). Comparison between vertical velocity DC and true DC (b). Comparison between the combination of pressure DC and vertical velocity DC with true DC (c).

One should notice that the DCs presented in Figure 22 do not guarantee perfect inversion results. Small changes in bottom parameters tend to cause tiny changes in the DC shape, which can be comparable to the errors imposed by the technique used to retrieve them, like reassigned spectrogram and ridge function used in this chapter. To exemplify that, Figure 23 zooms in two regions of mode 10 shown in Figure 22.

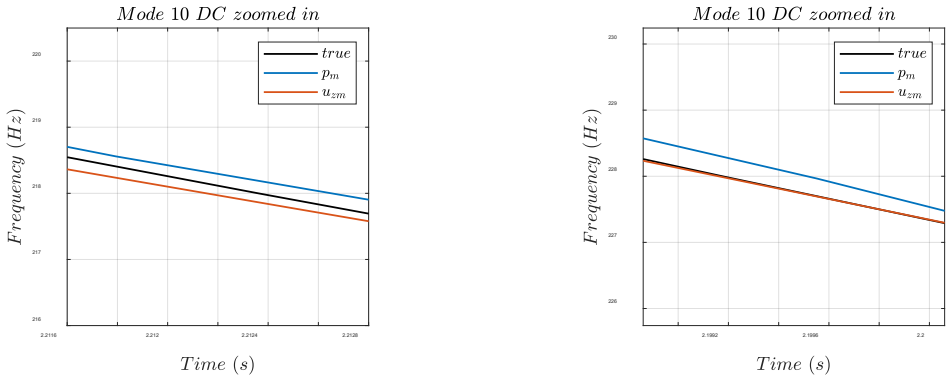

(a) (b)

Figure 23. Two regions of mode 10 DC extracted from Figure 22. Region where the DC averaging helps since the true DC is approximately half-way between pressure and vertical velocity (a). Region where the DC averaging does not help, the vertical velocity DC in this case is the best option (b).

Figure 23(a) illustrates one region where DC averaging can improve results, whereas Figure 23(b) presents a region where vertical velocity is a better option. Since in real world application there is no reference to compare with and considering that a full retrieved DC possesses many regions where averaging helps, but others where it does not help, the results presented ahead will show if the net contribution of averaging is worth the increasing cost in signal processing.

In the case of the DC obtained using RAM full-field predictions, Figure 24(a) shows the use of a binary mask and Figure 24(b) shows the use of a band-pass filter mask, using TW to separate the modes.

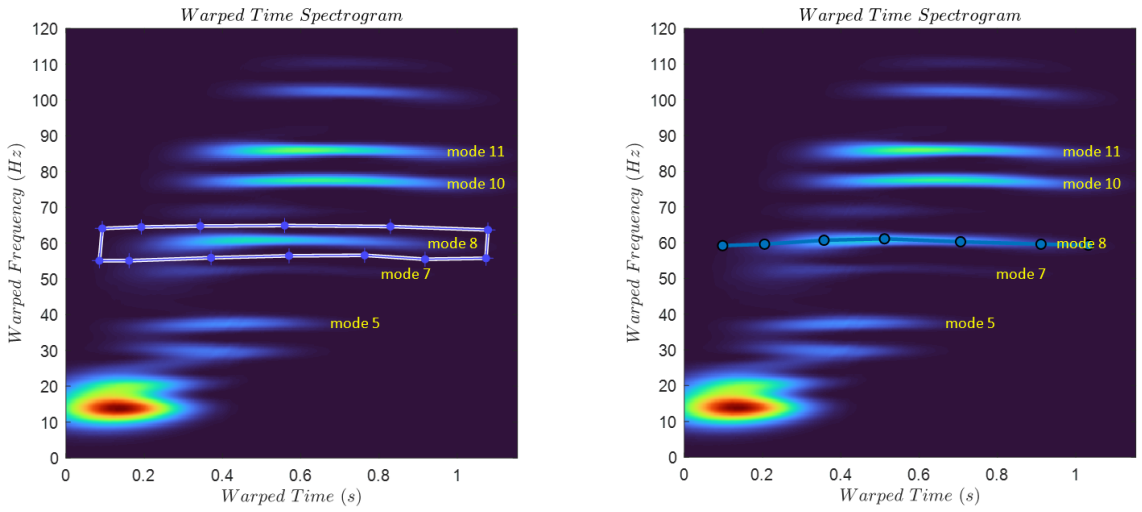

Figure 24. Warped-domain spectrogram. A binary mask is used, which applies rectangular windows of different sizes to each column of the warped-domain Short-time Fourier transform matrix (a). A band-pass filter mask is used, which applies a band-pass filter with constant bandwidth to each column of the warped-domain Short-time Fourier transform matrix (b).

A binary mask, to be referred to as TRAD mask, applies rectangular windows of different sizes to each column of the warped-domain Short-time Fourier transform (STFT) matrix. The consequent abrupt transition in the frequency-domain causes distortions in the time-domain. In 2021, Guarino *et al.* [9] proposed a band-pass filter mask approach, to be referred to as BPF mask, which improved results substantially. Another benefit of the BPF mask is that it makes it easier to mask the mode in a more precise way, depending less on the ability of the operator, which is required when using TRAD mask [1]. For that reason, the BPF mask is used in this chapter.

Additionally, to minimize errors, each mode is masked four times and the average DC is taken. Figure 25 shows the DCs obtained using BPF mask, including modes 5,7,8,10, and 11.

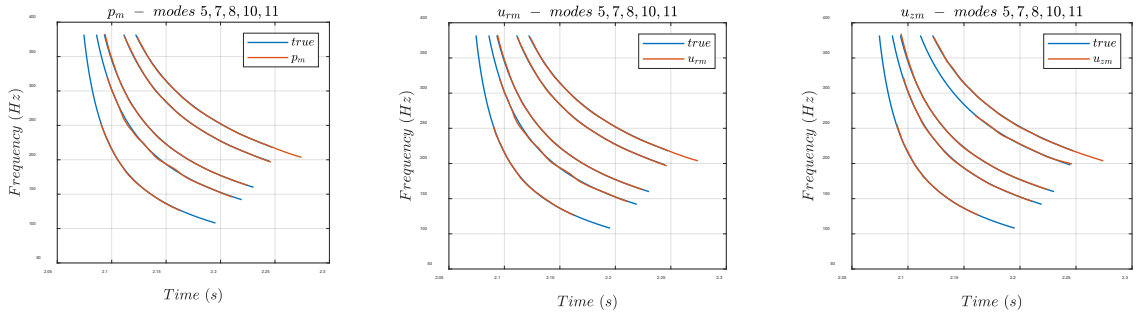

(a) (b) (c)

Figure 25. RAM based DCs, separated with TW and BPF mask using pressure signal (a), using radial velocity signal (b), and using vertical velocity (c).

Finally, the optimization tools are based on MATLAB function "ga" [34] within the Global Optimization Toolbox and on function "bayesopt" [35] within the Statistics and Machine Learning Toolbox.

The uncertainties of the preliminary analysis using synthetic signals are estimated using the MATLAB Bayesian Optimization object, which connects to the function "predictObjective" [36] that in turn provides the standard deviation around the minimum predicted estimate, using the posterior distribution of the Gaussian process model. The geoacoustic parameters uncertainties are estimated as follows: the standard deviation (σ) calculated using the function "predictObjective" is added to the point with the lowest cost function score, defining a threshold as shown in Figure 26(a) by the black dashed line. All points (vectors) with cost function score lower or equal to the threshold are taken. Within those points, the root-mean-square (RMS) is calculated and the uncertainty is estimated as illustrated in Figure 26(b). The procedure is applied to estimate all geoacoustic parameters uncertainty as shown in Figure 26(c–e).

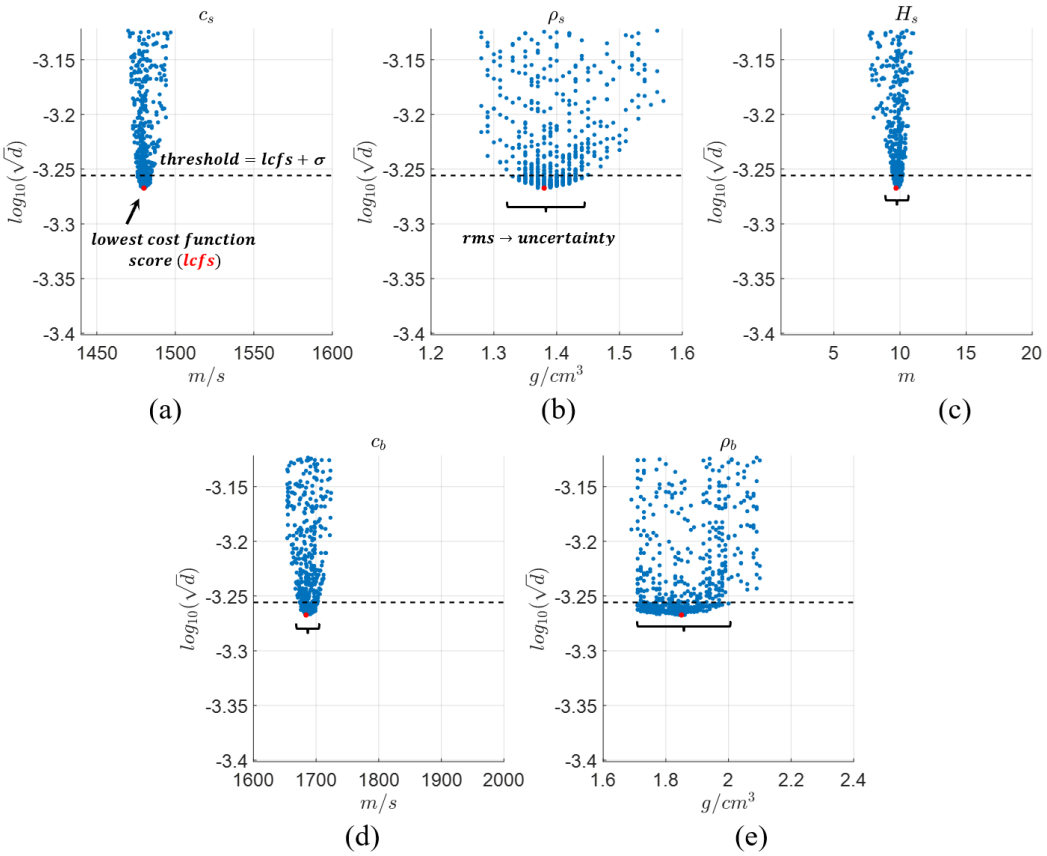

Figure 26. Example of optimization scatter plots when white noise is added to the RAM pressure signal at a signal to noise ratio of 20 dB and TW is applied to separate the modes using BPF mask. In the y-axis, d is the result of Equation 32. The threshold is obtained adding to the lowest cost function score the standard deviation obtained using the MATLAB function "predictObjective" (a). The geoacoustic parameter uncertainty is calculated considering all points below the threshold represented by the dashed line (b). The same procedure is applied to estimate all geoacoustic parameters uncertainty. c_s is the sediment sound speed (m/s), ρ_s the sediment density (g/cm^3), H_s the sediment thickness (m), c_b the sub-bottom sound speed (m/s), and ρ_b the sub-bottom density (g/cm^3) (c–e).

Finally, Figure 27 shows the inversion results using synthetic signals including the channels combinations and using BPF mask at the following signal-to-noise ratios: ∞, 20, and 10 dB. In addition, "KRAKEN mode waveform" approach is included to provide results without the influence of TW. Still, the SNRs 25 and 15 dB are not included, since the results are similar to the other SNRs tested.

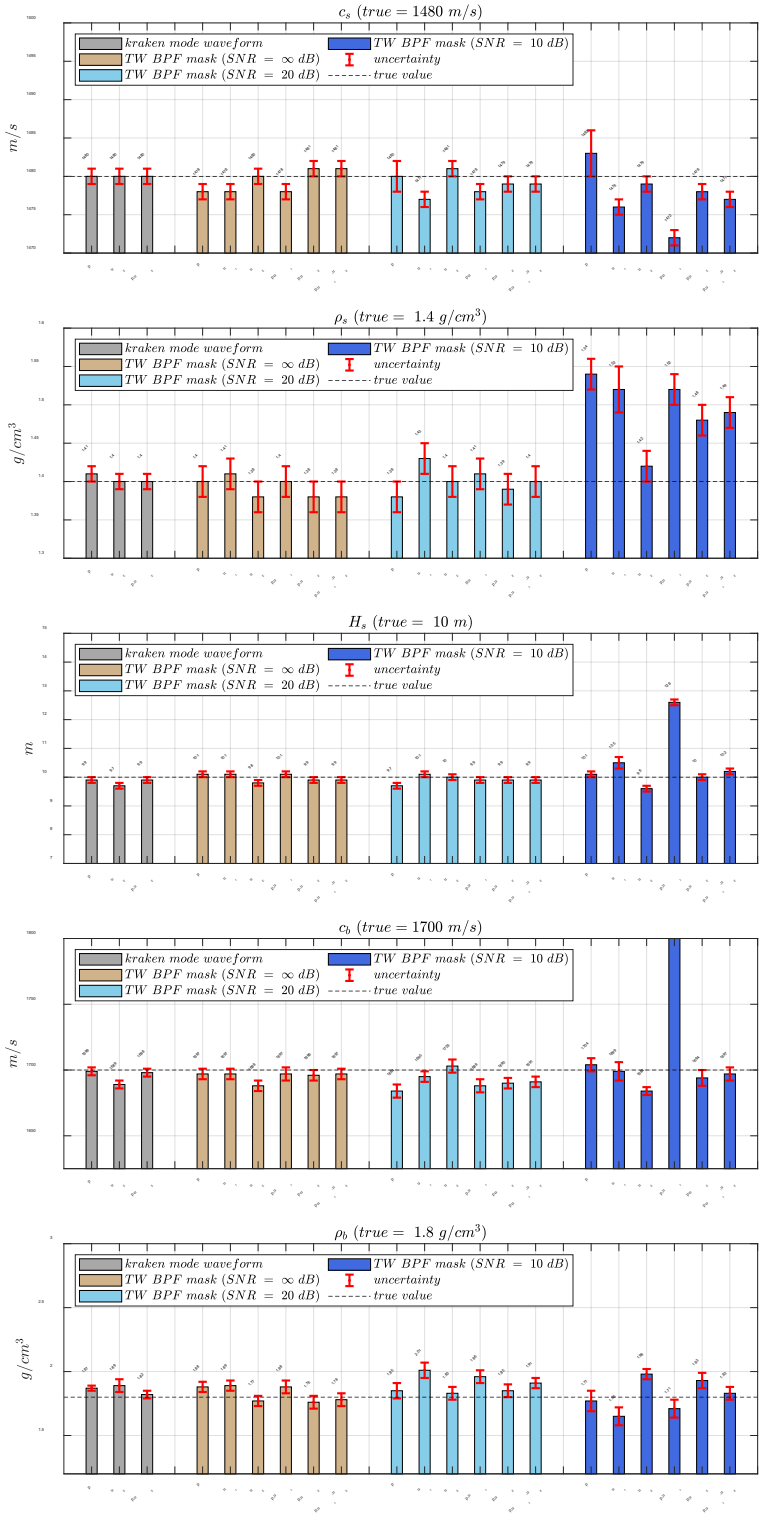

Figure 27. Estimated geoacoustic parameters using synthetic signals. “KRAKEN mode waveform” presents results without the influence of TW. The remaining results are RAM based with white noise included at the ratios ∞, 20 and 10 dB, applying TW to separate the modes using BPF mask.

First, Figure 27 shows that when the SNR is lowered, the geoacoustic parameters estimation gets worse, which is an expected behavior. It still shows that 20 dB represent a reasonable SNR to obtain better results, which is easily achievable using explosive (e.g., SUS) or implosive (e.g., light bulbs) sources.

Second, the uncertainty of "KRAKEN mode waveform" is a bit lower, especially for ρ_s, c_b and ρ_b, which indicates that TW tends to increase the uncertainty of the estimated parameters. When the SNR is low, an analogous behavior is observed. Such behavior suggests the worse the DC quality to be matched by the optimization process, the higher the uncertainty of the results, which makes sense.

Third, TW slightly increases the results variance, and the worst case is observed at the lowest SNR.

Next, a comparison is made between TRAD mask and BPF mask results for noiseless situation. Figure 28 shows the percentage error between estimate and true value for each geoacoustic parameter. The BPF mask improves c_b estimation and has some positive effect on H_s and ρ_b as well. Figure 29 presents the RMS percentage error calculated over all geoacoustic parameters percentage errors of Figure 28.

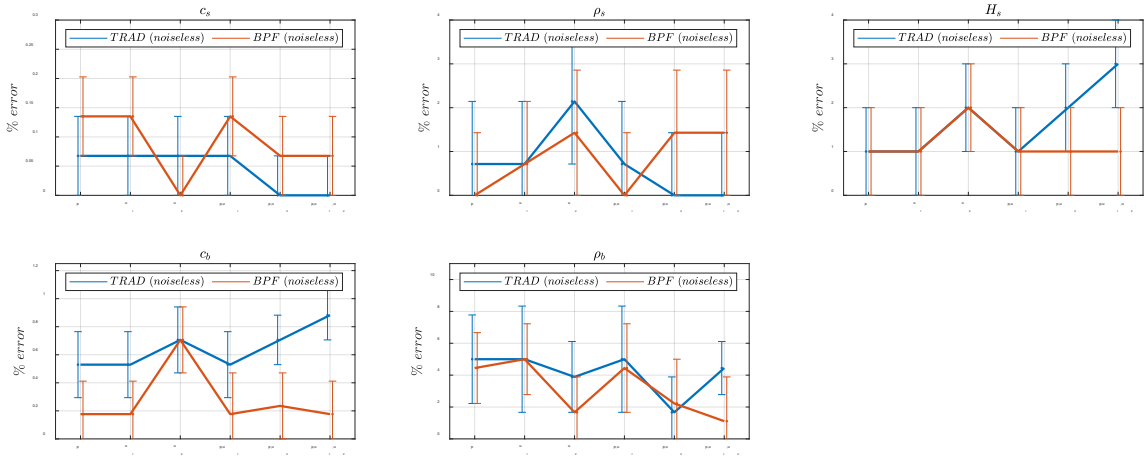

Figure 28. Comparison between TRAD mask and BPF mask for noiseless situation, considering the percentage error between estimate and true value.

Figure 29 indicates that the BPF mask improves results over the TRAD mask. If the average is taken over all combinations of Figure 29, the error decreases by a factor of 1.3.

Figure 29. Comparison between TRAD mask and BPF mask for noiseless situation, considering the RMS percentage error calculated over all geoacoustic parameters percentage errors of Figure 28.

Figure 30(a,b) illustrate the RMS percentage error for SNR ∞ and 20 dB, using BPF mask and including all combinations of channels. Figure 30(b) shows that pressure and vertical velocity produce better results, and Figure 30(c) confirms that the combination of p, u_z is more stable and the best choice, with a modest improvement over pressure-only method. The same result applies to "KRAKEN mode waveform," which indicates that the combination of p, u_z helps to mitigate the distortions caused using reassigned spectrogram and ridge function.

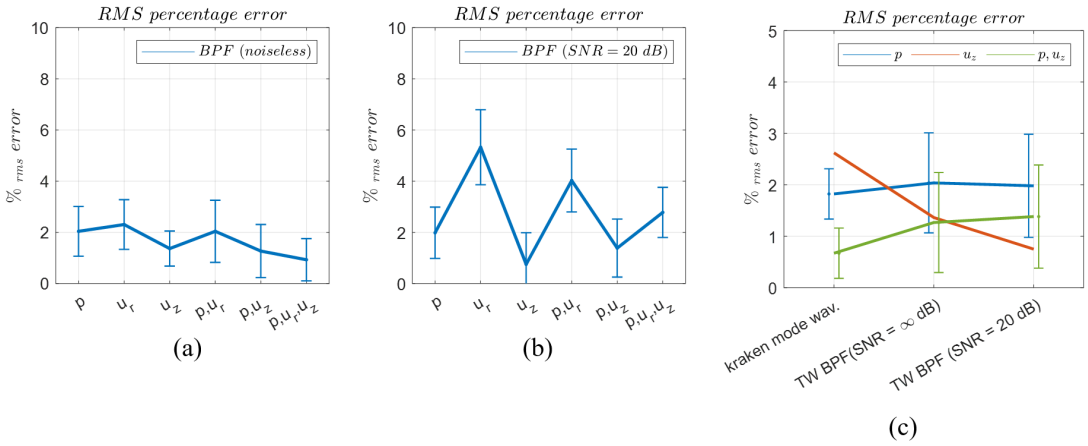

Figure 30. Inversion performance using BPF mask. Results without noise (a). Results show that the vertical velocity improves error (b). Results confirm that the combination p, u_z is more stable and the best choice, with a modest improvement over pressure-only method (c).

3. Inversion of Sea Test Data

The results of the preliminary analysis using synthetic signals showed that the BPF mask performs at least the same as or better than the TRAD mask. Therefore, only the BPF mask is used to evaluate the sea test data.

First, the DC retrieval using sea test data follow the same procedure of the synthetic signals. To illustrate the shots waveforms, Figure 31 shows both shots including pressure (p) and horizontal velocity (u_x), and vertical velocity (u_z).

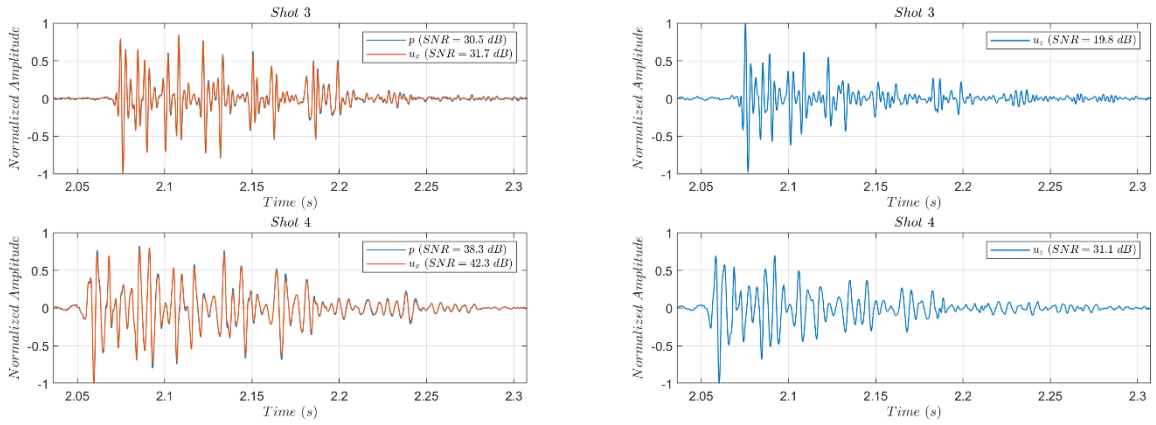

Figure 31. Vector sensor shots 3 and 4 collected data. On the left pressure (p) and horizontal velocity (u_x), and on the right vertical velocity (u_z). The plots include the SNR of each signal.

All channels have high SNR. The calculation was done taking the RMS value right before the signal, for noise calculation, and including the signal until ~2.2 s. In both cases, the vertical velocity channel is the noisiest compared to the other channels, but still with good SNR of 19.8 and 31.1 dB, respectively. To improve the separation of modes in the warped-domain, according to Duan *et al.* [26], source deconvolution is applied. Figure 32 illustrates the deconvolved pressure signals for shots 3 and 4. For the sake of representation, shot 4 is shifted to the right to match shot 3's position, since shot 4 has a shorter range. Figure 33 illustrates the respective spectrograms in the warped-domain.

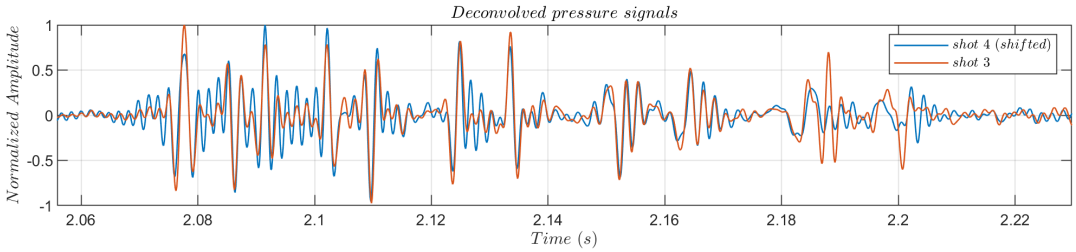

Figure 32. Deconvolved pressure signals for shots 3 and 4.

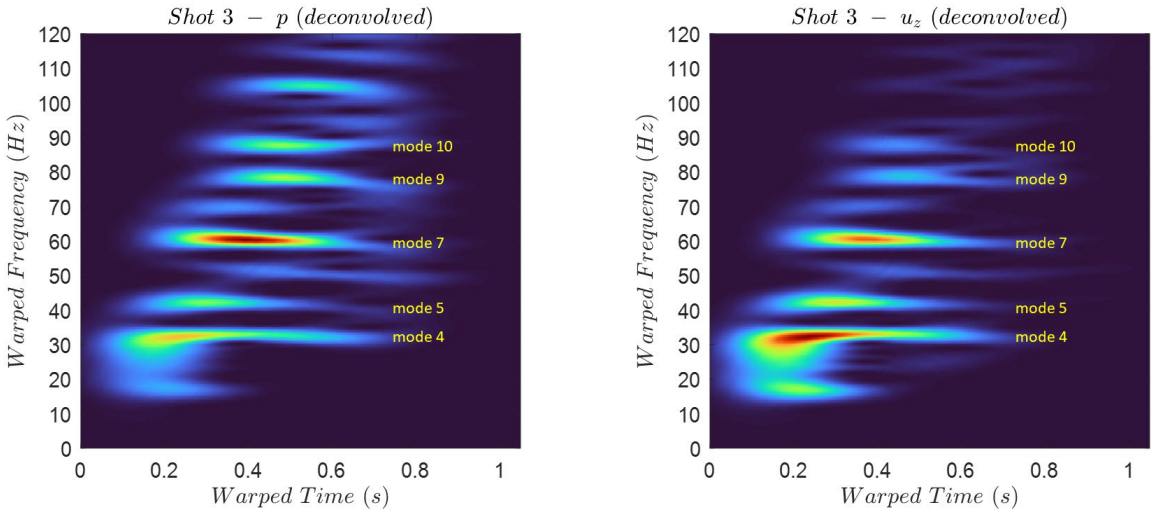

(a) (b)

Figure 33. Shot 3 deconvolved signals warped-domain spectrograms: pressure (a) and vertical velocity (b).

The spectrograms of Figure 33 present higher intermodal interference in the warped domain compared to the synthetic signal spectrogram showed in Figure 24, which affects the DC retrieval capabilities and the duration of the retrieved DC in time as illustrated in Figure 34(a), especially for modes 9 and 10. Figure 34(b) zooms in modes 4 and 5 DC.

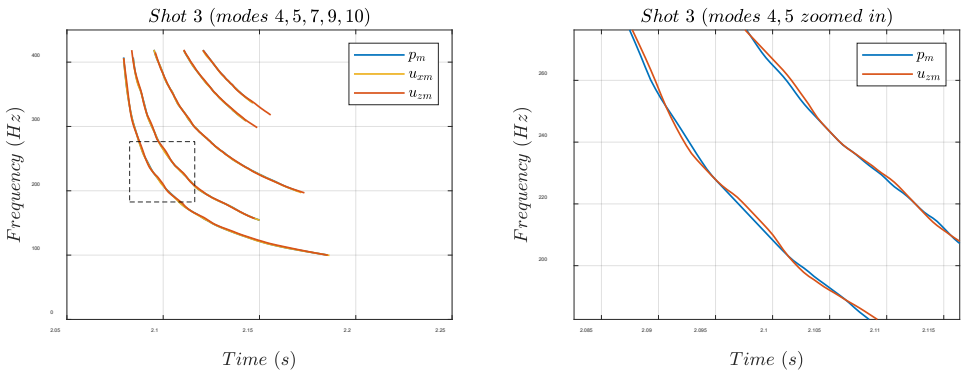

(a) (b)

Figure 34. Shot 3 DCs retrieved using BPF mask, including modes 4, 5, 7, 9, 10. Pressure (p), horizontal velocity (u_x), and vertical velocity (u_z) (a) . Modes 4,5 DC zoomed in (b).

The inversion is calculated using the most stable portions of the DC considering modes 4, 5, 7, 9, 10, as shown in Figs. 33 and 34. In addition to the geoacoustic parameters c_s , ρ_s , H_s , c_b , ρ_b, three other parameters are included in the inversion: sediment sound speed gradient (∇c_s), range (R), and time shift (dt) as shown in Equation 32 to account for range mismatches.

The geoacoustic parameters uncertainty estimation follows the same procedure shown in Figure 26, which is based on travel time uncertainty, but the threshold here is obtained using the mode travel time measurement in the actual experiment, with different contributions like ambient noise, for instance. Since each mode is selected with four different masks, the travel time uncertainty is then estimated using the RMS difference among the four DC of the same mode, for each frequency bin, and then averaged over all frequencies and all modes. The results indicate that the BPF mask decreases the uncertainty of the velocity channels, bringing it down to the pressure channel uncertainty level.

The geoacoustic inversion results are presented in Figure 35, where dark blue indicates pressure and orange indicates combination of pressure DC and vertical velocity DC, for both shots 3 and 4.

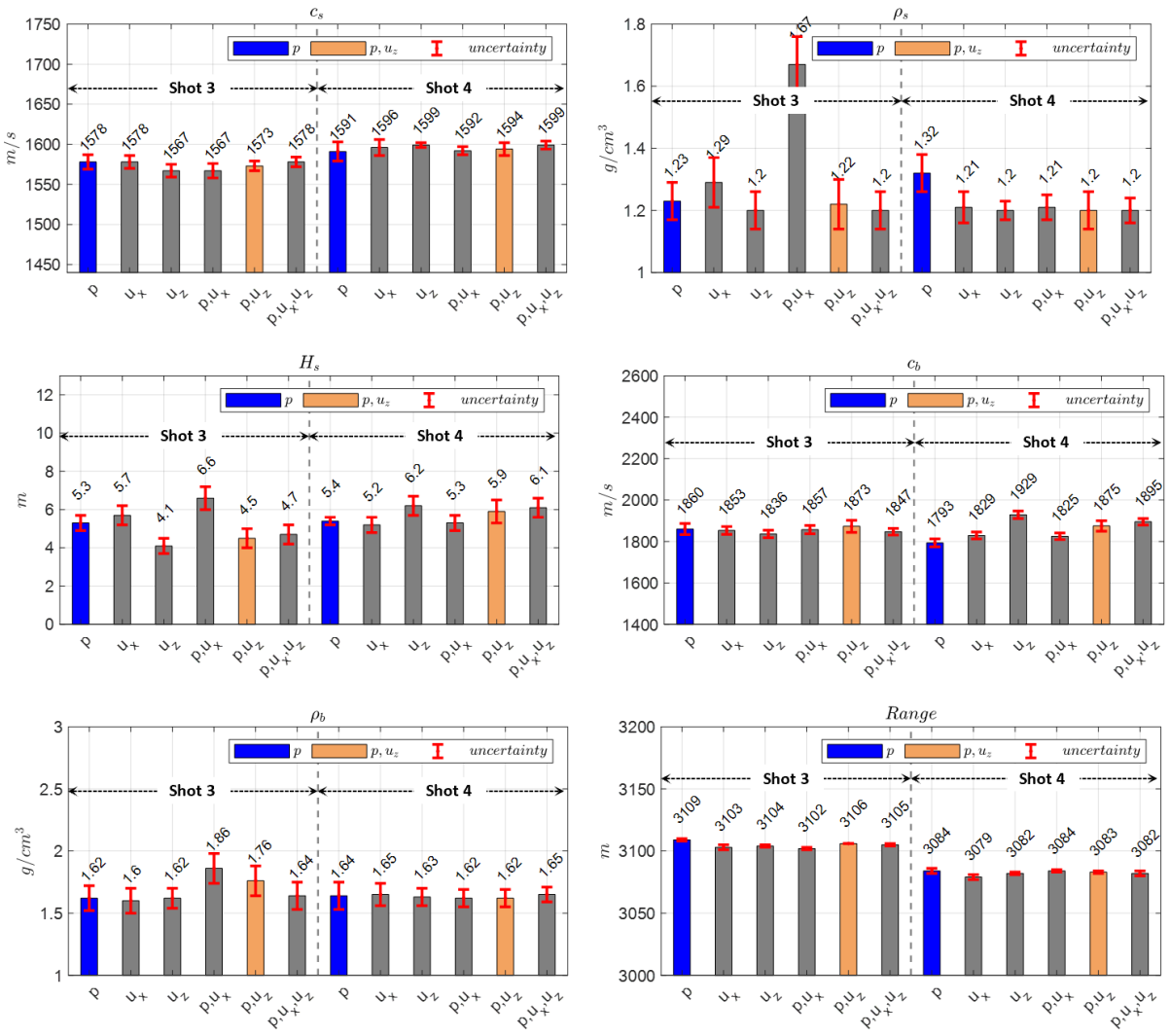

Figure 35. Estimated geoacoustic parameters using shots 3 and 4 data. Dark blue indicates pressure and orange indicates combination of pressure DC and vertical velocity DC, where BPF mask is used in TW to extract de modes.

Figure 35 does not present the estimation of sound speed gradient. The results were highly variable, and the overall inversion improved when no gradient was considered.

D. DISCUSSION

This chapter presents a multichannel geoacoustic inversion technique based on DCs averaging using data collected in Monterey Bay in 2019. The motivation is to utilize additional statistics, especially since the observations are limited to only two light bulb implosions. The implementation of two forward models (KRAKEN, RAM) allowed us to investigate and compare their accuracy to predict components of the vector field in a range dependent environment. Linking the number of range segments to the bathymetry maximum vertical step using KRAKEN allowed for good matching with RAM's predictions as shown in Figure 21.

RAM required TW to separate modes and we compared two different signal processing implementations to extract DC for processing. The BPF mask approach proposed by Guarino *et al.* [9] reduced the velocity channels uncertainty and improved results for the estimation of bottom attenuation coefficient. Results in conjunction with [9] suggest that the TRAD mask should not be the first choice when TW is required. The mode masking procedure in TW was chosen to be the major source of uncertainty for data since the selection of modes is very subjective, depending on the operator's ability.

The synthetic analysis suggests that the DC estimated from the vector sensor radial velocity channel does not improve the inversion [Figure 30(b)], largely because pressure and radial velocity waveforms tend to be very similar. Figure 31 illustrates this similarity.

The vertical channel offers added value for some data-parts to improve parameter estimates. The synthetic analysis suggests a positive net contribution of averaging pressure and vertical velocity DCs to reduce distortions caused by the reassigned spectrogram and ridge function, as shown in Figure 30. Without TW the improvement is even more significant and reduces uncertainty [Figure 30(c)]. With TW a modest improvement is still observed yet with increased uncertainty.

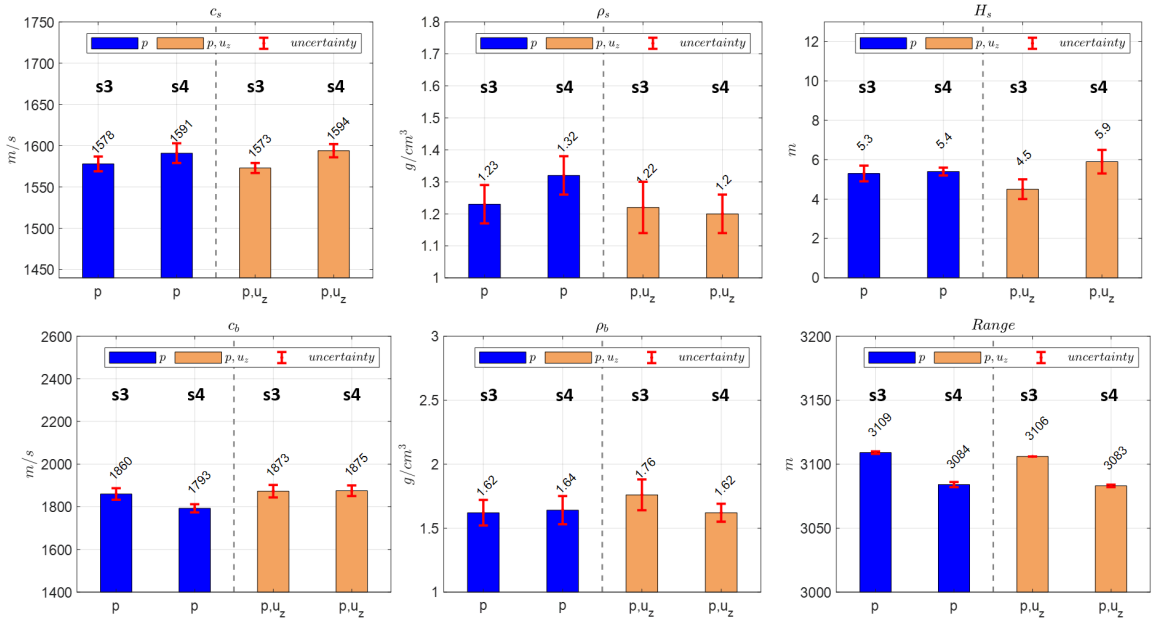

Figure 36. Estimated geoacoustic parameters using shot 3 (s3) and shot 4 (s4) data. Only results for p and p, u_z combination is presented.

Data results in Figure 36 present estimated parameters for the channel combinations p and p, u_z. Overall, Shots 3 and 4 present similar results due to the high SNR of both light bulb implosions and the range is estimated consistently. Considering p, u_z combination, the range estimation for Shot 4 is 3083 m (GPS 3065 m) and for Shot 3 is 3106 m (GPS 3090 m). The differences of 18 m and 16 m, respectively, are comparable to the distance between the GPS antenna location in the boat and the location where the light bulb was deployed. Those differences also account for the uncertainty associated with the vector sensor's exact location on the seafloor. Figure 37 shows the synthetic results for SNR 25 and 20 dB using BPF mask to help with the interpretation of Figure 36 results.

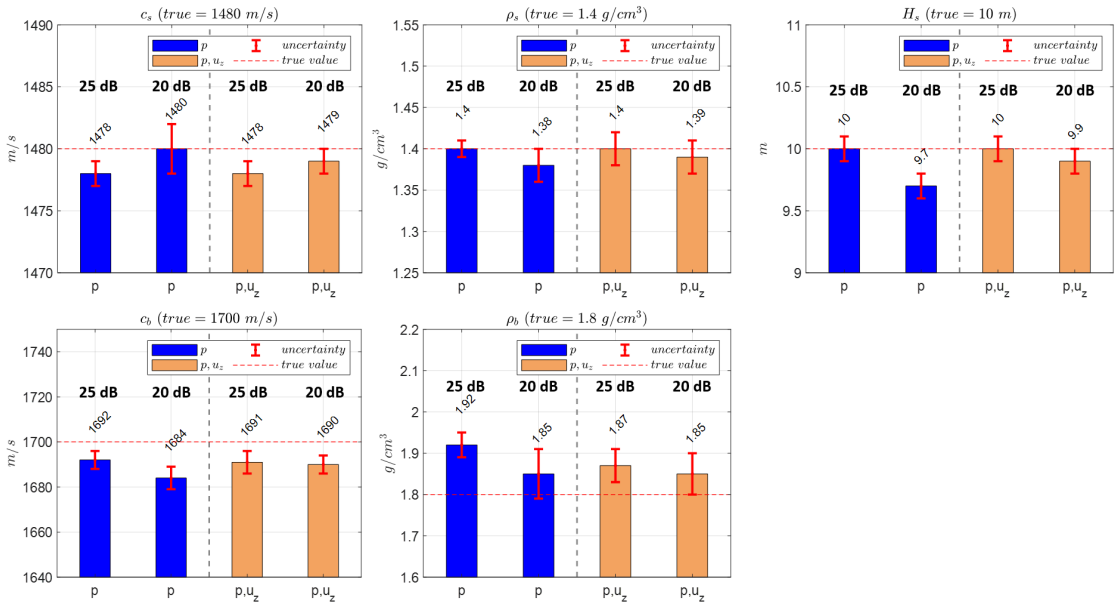

Figure 37. Estimated geoacoustic parameters using synthetic signals, SNR 25 and 20 dB and BPF mask. Only results for p and $\mathrm{p, u_z}$ combination is presented.

The combination p, u_z for the synthetic results of Figure 37 have lower variance compared to pressure-only, which does not apply to all parameters for the at-sea test data in Figure 36. One explanation for the increased variance is a changing intermodal interference in the warped-domain. It is difficult to exactly quantify that effect on the limited number of data points in this work; yet, results in Figure 36 demonstrate that data from the vertical channel is similar to the pressure data and thus can reduce uncertainty in the parameter estimates. Since each geoacoustic parameter has a different effect on the DC shape, a multi-channel combination can be beneficial for some parameters estimation, but potentially not for all. Table 2 shows the final geoacoustic inversion estimation.

Table 2. Geoacoustic inversion final parameters estimation using sea test data.

	Pressure-only results		Combination of pressure and vert. velocity results		Final parameter estimates		
	mean	std deviation	mean	std deviation	mean	std deviation	selected combination
c_s (m/s)	1585	8	**1584**	**5**	1584	5	p,u_z
ρ_s (g/cm^3)	1.28	0.04	**1.21**	**0.05**	1.21	0.05	p,u_z
H_s (m)	**5.4**	**0.3**	5.2	0.4	5.4	0.3	p
c_b (m/s)	1827	16	**1874**	**19**	1874	19	p,u_z
ρ_b (g/cm^3)	**1.63**	**0.07**	1.69	0.07	1.63	0.07	p

E. CONCLUSION

This chapter investigated the hypothesis that the multichannel DC averaging adds value to the conventional pressure-only analysis. Sea test data and synthetic predictions using models KRAKEN and RAM were adopted, TW used to separate modal arrivals, and a hybrid optimization approach included. We show that the combination of pressure and vertical velocity DCs can improve parameter estimates, and lower results variance. We also looked at the band-pass filter masking approach for modal separation, which indicated that the traditional binary mask should not be the first choice when TW is required.

THIS PAGE INTENTIONALLY LEFT BLANK

IV. IMPROVEMENTS USING WAVEFORM MATCHING

This chapter is based on the manuscript [11] (*Geoacoustic inversion using waveform matching as a preliminary step in dispersion curve analysis to assess bottom attenuation from a single vector sensor*) that was submitted for publication in the *International Congress on Acoustics* (ICA2022) on May 12, 2022. The manuscript is under review with the number ABS-0288.

A. INTRODUCTION

In shallow water ocean waveguides, sound propagation presents a dispersive behavior, being greatly influenced by the ocean bottom properties. Such behavior is represented by DCs, which reflect the dependency of normal mode travel time with frequency, the most broadly used feature [1], [2], [14] in ocean remote sensing for the geoacoustic inversion of environmental parameters. Normal mode properties can be identified using different approaches, and TW is one that has been increasingly adopted by the acoustics community for modal separation. It is a technique that relies on one sensor using broadband signals, which simplifies the at-sea probing task. Bonnel *et al.* present details about TW in [1].

Despite being very popular, DC inversion techniques suffer from intrinsic errors and distortions associated with normal mode separation via TW methods, such as (1) the lack of high resolution in time-frequency analysis, (2) the use of an imperfect TW operator based on the ideal waveguide, which affects performance in more complex environments, and (3) the abrupt transitions included in the processing caused by rectangular windows applied both in the time-domain, before the warping transformation, and in the time-frequency domain using binary masks. Some approaches have been proposed to attenuate such distortions, like the use of a band-pass filter (BPF) mask [9] and utilization of additional acoustic channels included in vector sensors.

Many researchers have studied vector sensors in geoacoustic inversion, beyond their application in direction finding or target tracking. In 2021, Guarino *et al.* [9] showed that the modal phase difference between pressure and vertical velocity can be a possible

candidate for the estimation of the bottom attenuation coefficient. This has been traditionally estimated, for example, using pressure-only sensors and mode amplitudes, as done by Duan *et al.* [26] in 2016. In 2022, Guarino *et al.* [10] discussed the value added by doing multichannel averaging of pressure and vertical velocity DCs to reduce distortions.

This chapter expands the analysis done in [10]. The former study investigated the averaging hypothesis using synthetic signals and data collected on a single vector sensor deployed on the northern shelf during the Monterey Bay 2019 experiment. The inversion showed that the combination adds value to the pressure-only analysis and improved results.

This work uses the same data and environmental model of [10]. The inversion utilizes sound speed profiles measured during the test event and assumes a sediment layer of constant thickness overlying a deeper sub-bottom type. Since data can be contaminated by other sources of error like noise and mode coupling, these effects can worsen DC quality even more. In this context, this chapter discusses the value added by using waveform matching [37] as a preliminary step to improve the performance of the DC inversion. The chapter shows that waveform matching can provide a way to check the DC quality and improve DC inversion. It is also shown that waveform matching results can be refined with simultaneous matching of pressure and vertical velocity waveforms, and using the modal phase difference for better estimates of bottom attenuation.

To show this, the KRAKEN [7] normal mode model is applied for synthetic predictions, which include DCs based on group speed, and full-field and individual mode predictions for both pressure and vertical velocity using the adiabatic approximation. To guarantee optimum results, KRAKEN is first calibrated using the parabolic equation model RAM [8] as a reference.

As for the optimization approach, the same structure is used as in [10]. Genetic algorithms (GAs) can rapidly locate the global optimum; however, it can be slow to locate the exact local optimum in the region of convergence. A hybrid optimization approach is implemented to expedite convergence.

This chapter is organized as follows: the sea test characteristics, environmental model and DC inversion scheme are briefly explained, and details can be found in [10]. The inversion scheme for waveform matching is defined. Next, DC inversion is applied using the multichannel combination of pressure and vertical velocity and band-pass filter mask (BPF) using TW, as shown in [10] to be the best option. Waveform matching is then applied individually for pressure and vertical velocity data, and for both signals simultaneously. After that, the modal phase difference approach is presented and used to refine the waveform matching outcomes. The estimated parameters from both DC inversion and waveform matching inversion are used to generate synthetic DC, and such replicas are compared with the DC from data to evaluate the quality of the DC inversion.

The results show that in the case of this chapter, waveform matching inversion performs better than the DC matching inversion, supported by the modal phase difference approach and simultaneous matching. The manuscript concludes with our analysis of experimental data followed by a discussion of results.

B. SEA TEST CHARACTERISTICS AND ENVIRONMENTAL MODEL

This section presents a description of the sea test characteristics and environmental model. More details can be found in [10]. The acoustic data was collected in 2019 in Monterey Bay. Figure 38(a) shows a bathymetric map of the experiment location. The location of two yellow markers labeled Shot 3 and Shot 4 correspond to two light bulb [Figure 38(b)] implosions. The environmental model assumes a sediment layer of constant thickness overlying a deeper sub-bottom type, as illustrated in Figure 38(c).

Prior information from two CTD casts are used in this work: CTD6 and CTD5 are taken at the vicinity of the source (light bulb) and receiver (vector sensor). A reference hydrophone near the source was used, which allowed us to estimate the source depth for Shots 3 and 4 of 29.8 and 29.7 m, respectively. A Geospectrum M20-105 vector sensor system was used in the sea test. The sensor itself was suspended from the frame with a nylon rope as shown in Figure 38(d). The system frame was place on the seafloor at ~85 m depth [Figure 38(c)]. To mitigate flow noise, the system was covered prior to the deployment with a fabric.

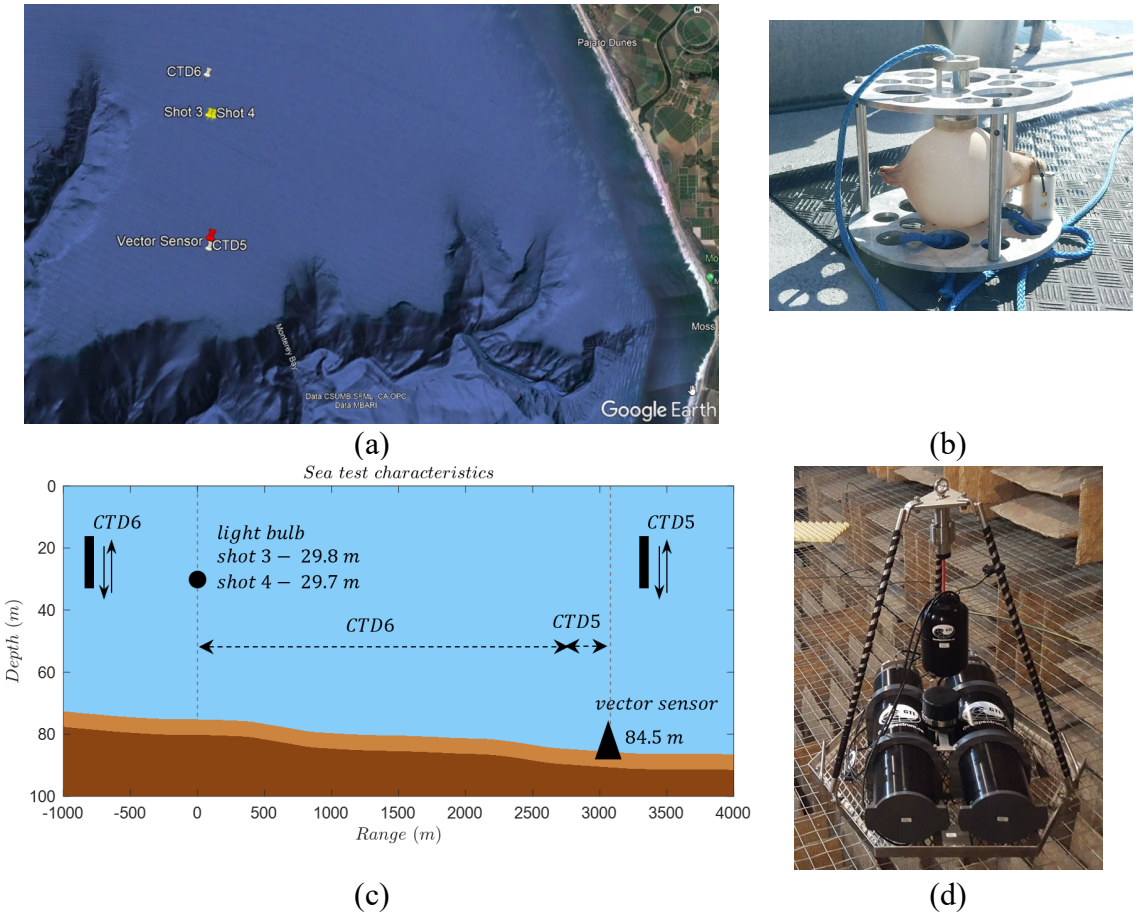

Figure 38. Overall sea test characteristics. Location of the test event in Monterey Bay, showing the positions of the two light bulb implosions in yellow, CTD castings in white and vector sensor in red (a). Light bulb system setup. The implosion is carried out sending a messenger from the boat that travels along the rope and breaks the light bulb (b). Range dependent environmental model used in the analysis (c). Vector sensor system used in the sea test, model GTI M20-105 (d).

As for the effective bottom model [3], the sub-bottom has constant sound speed, density and attenuation coefficient, whereas the sediment layer has all parameters constant except for the sound speed that has a constant gradient. Regarding ground truth information [3], the bottom is composed mainly by mud, very fine sand, and silt according to the California Seafloor Mapping Program [31].

C. INVERSION METHODS

The inversion methods use DCs directly computed by KRAKEN group speed, and full-field and individual mode predictions, which are used for waveform matching and phase difference approaches, applying an adiabatic approximation. Since KRAKEN is a normal mode model, the number of range segments is determined based on the constraint that the maximum bathymetry vertical step must be less than or equal to the highest frequency component wavelength, as shown in [10]. Figure 39 shows a comparison between KRAKEN and RAM for calibration purposes for a certain set of environmental parameters, according to Figure 38(c).

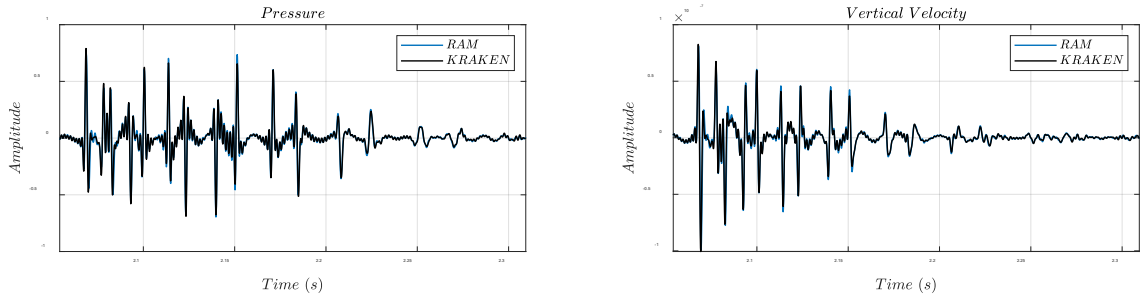

Figure 39. Comparison between KRAKEN and RAM for a certain set of environmental parameters according to Figure 38(c). Both waveforms match consistently for calibration purposes.

The hybrid optimization approach applies two genetic algorithm (GA) instances followed by two Bayesian optimization instances, where the lower and upper bounds of each searched parameter shrink accordingly as the optimization process moves forward. The optimization tools are based on the MATLAB function "ga" [34] within the Global Optimization Toolbox and on the function "bayesopt" [35] within the Statistics and Machine Learning Toolbox.

The cost function d for the DC inversion is based on the minimization of the mean squared error average between the DC estimate, which is calculated from data, and DC replica travel times with frequency being the independent variable according to

$$d = \frac{1}{M}\sum_{m=1}^{M}\frac{1}{N_m}\sum_{i=1}^{N_m}\left[\hat{t}_m(f_i) - t_{m_r}(f_i) + dt\right]^2 , \tag{33}$$

where M is the number of modes, N_m is the number of points of a specific mode DC, $\hat{t}_m$ is the DC estimate travel time, t_{m_r} is the DC replica travel time and dt is a time shift included as a search parameter when the sea test signals are used to compensate for small range mismatches. The cost function $\hat{d}$ for the waveform matching is defined as

$$\hat{d} = \sqrt{\frac{1}{M}\sum_{i=1}^{M}\left[y[i+N] - y_r[i]\right]^2}\ \left(1 - \frac{|y^T . y_r|}{|y||y_r|}\right), \tag{34}$$

where y is data (pressure or vertical velocity), y_r is the replica, and N is a shift included as a search parameter to account for range mismatches. The first term is the root mean square error (RMSE) and the second term includes the correlation coefficient. The calculation is done using only the portion of data where signal is present. The choice for both terms allows for replicas that do not match perfectly, working as a balance between both calculations, with the first part mostly matching amplitude, and the second part mostly matching phase. This approach was found useful for the employed reduced order bottom model.

D. INVERSION OF DATA USING DCS

Data is inverted using shots 3 and 4. Both shots have high SNR for pressure and vertical velocity signals. To illustrate, considering shot 4 the SNR values are 38.3 dB and 31.1 dB, respectively. To improve the separation of modes in the warped-domain, according to Duan *et al.* [13], source deconvolution is applied. Details about the pressure and vertical velocity full-field and deconvolved signals can be found in [10]. The modes are then separated using TW with a BPF mask, as shown in Figure 40(a) for the pressure signal while Figure 40(b) shows the warped-domain spectrogram for the vertical velocity signal, and Figure 40(c) shows the pressure and vertical velocity retrieved DCs.

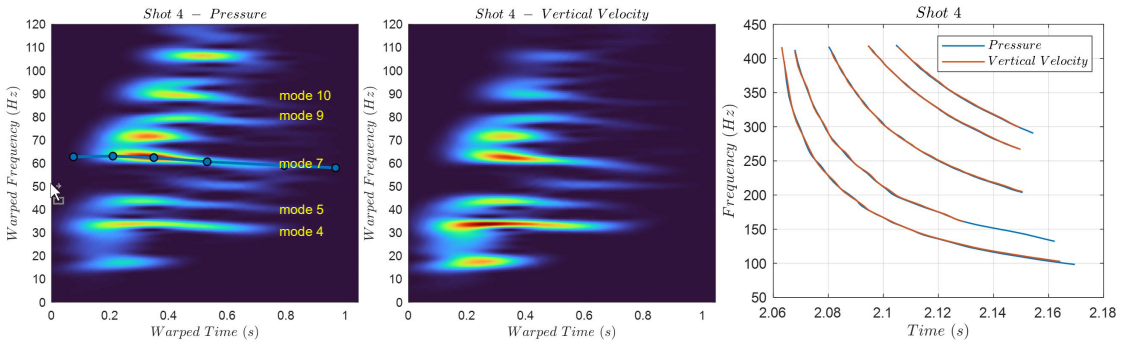

(a) (b) (c)

Figure 40. Shot 4 data. Warped-domain spectrogram for deconvolved pressure signal using BPF mask (a). Warped-domain spectrogram for deconvolved vertical velocity signal (b). Deconvolved pressure and vertical velocity retrieved DCs for modes 4, 5, 7, 9, 10 (c).

The warped-time spectrograms and DCs for shot 3 can be found in [10]. Table 3 shows the inverted parameters for shots 3 and 4, and Figure 41 shows the DCs and the full-field collected data compared with Table 3's shot 4 replica.

Table 3. Inverted parameters for shots 3 and 4 using the combination of pressure and vertical velocity DCs.

	$\mathbf{c_s}$ (m/s)	$\nabla\mathbf{c_s}$ (m/s/m)	$\boldsymbol{\rho_s}$ (g/cm^3)	$\mathbf{a_s}$ (dB/m/kHz)	$\mathbf{H_s}$ (m)	$\mathbf{c_b}$ (m/s)	$\boldsymbol{\rho_b}$ (g/cm^3)	$\mathbf{a_b}$ (dB/m/kHz)	**range** (m)
Shot 3	1574	8.5	1.29	x	5.0	1914	2.00	x	3100
Shot 4	1577	7.5	1.32	x	6.4	1773	1.60	x	3083

c_s and c_b are the sediment and sub-bottom sound speeds (m/s), ∇c_s is the sediment sound speed gradient $(m/s/m)$, ρ_s and ρ_b are sediment and sub-bottom densities (g/cm^3), a_s and a_b are the sediment and sub-bottom attenuation coefficients $(dB/m/kHz)$, and H_s is the sediment thickness (m).

The range estimates in Table 3 are different because shots 3 and 4 were taken at slightly different locations as shown in [10]. Figures 41(b,c) show that the parameters found using the DC inversion do not provide a good matching in the time-domain. It can be noticed in the same figure that the replica low order modes travel faster than the ones in data, which suggests, for example, that sediment sound speed is overestimated. This suggests that the DC inversion must be compared with waveform matching, results for

which will be presented in a subsequent section. Prior to that comparison, the next section presents the modal phase difference approach.

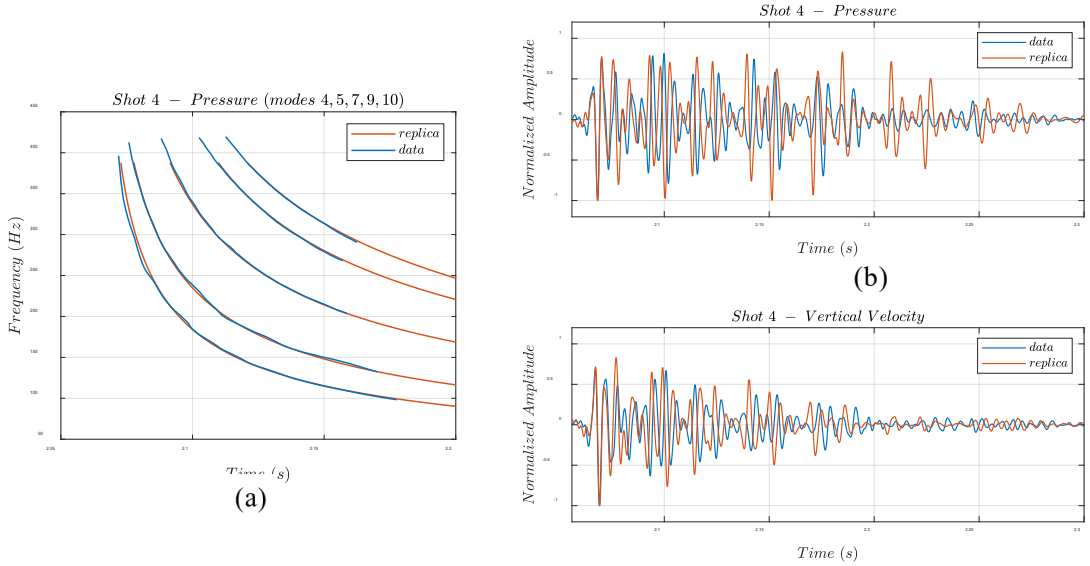

Figure 41. Comparison between data and replica for shot 4 inverted parameters. Pressure channel DCs for modes 4, 5, 7, 9, 10 (a). Pressure channel full-field (b). Vertical velocity channel full-field (c).

E. MODAL PHASE DIFFERENCE APPROACH

The modal phase difference is directly related to the modal attenuation coefficient. Following an analogous derivation as in [9], the modal pressure using the adiabatic approximation is given by [32, p. 410]

$$p_m(r,z) \approx \frac{j}{\rho\sqrt{8\pi r}}\; e^{-j\frac{\pi}{4}}\; \psi_m(0,z_s)\psi_m(r,z)\frac{e^{j\int_0^r k_m(r')dr'}}{\sqrt{k_m(r)}}. \tag{35}$$

The modal vertical velocity is obtained from the modal pressure gradient using the Euler equation

$$u_{z_m} = \frac{1}{j\omega\rho}\frac{\partial p_m}{\partial z}, \tag{36}$$

which is found to be

$$u_{z_m}(r,z) = \frac{p_m}{j\omega\rho}\frac{\frac{\partial\psi_m(r,z)}{\partial z}}{\psi_m(r,z)}. \tag{37}$$

The modal phase difference ($\Delta\theta$) can be obtained from the modal vertical intensity given by

$$I_{z_m}(r,z) = \frac{p_m\, u_{z_m}{}^*}{2} = j\frac{|p_m|^2}{2\omega\rho}\left[\frac{\frac{\partial\psi_m(r,z)}{\partial z}}{\psi_m(r,z)}\right]^* = A\, e^{j\Delta\theta}. \tag{38}$$

In the case of this chapter, the mode functions (ψ_m) are obtained using KRAKENC. However, since the propagation model has been updated to provide both full-field and individual mode components of pressure and vertical velocity in the time-domain, ultimately using MATLAB the calculation is done by

$$\Delta\theta = angle\left(fft(p_m).*\, conj\left(fft\left(u_{z_m}\right)\right)\right). \tag{39}$$

In the case of data, the modal phase difference is calculated in the same way as in Equation 39, based on the modal pressure and modal vertical velocity signals that are obtained using TW.

F. INVERSION OF DATA USING WAVEFORM MATCHING

The optimization using waveform matching applies the same hybrid optimization approach of the DC matching, except for the cost function that uses Equation 34. The inversion is done using shots 3 and 4, matching pressure and vertical velocity individually, and simultaneously using both signals. In the case of the simultaneous matching, Equation 34 is calculated for each signal, and then the results multiplied. Table 4 shows the inverted parameters.

Table 4 shows that the inverted values for shots 3 and 4 using pressure-only have good agreement, whereas using vertical velocity-only, some parameters seem to be overestimated (e.g., c_s, H_s, and a_b). The simplicity of the bottom effective model may be responsible for the increase in a_b, which ends up being correlated with other parameters that are equally erroneously estimated. Therefore, when it comes to the estimation of

sediment and sub-bottom attenuation coefficients, the results vary substantially. On the other hand, when simultaneous matching is applied, the results in bold have less variance. The modal phase difference between pressure and vertical velocity is then used to refine the results of Table 4. To illustrate that, shot 4's mode 5 is used and its waveforms for pressure and vertical velocity are separated from the full-field signals as shown in Figure 42. Next, the modal phase difference is calculated using Equation 39 and the results are shown in Figure 43 for shot 3 in blue and shot 4 in red. Next, KRAKEN is used to generate the individual modes for pressure and vertical velocity for each set of inverted values of Table 4. The phase difference is then calculated using Equation 39, and the results shown in Figure 43(a–f), where data and replica can be compared. $S4\ (p, u_z)$ is the overall best result. Figure 44 shows the comparison of waveforms between data and replica using $S4\ (p, u_z)$ inverted values.

Table 4. Inverted parameters for shots 3 and 4 using waveform matching.

	c_s (m/s)	∇c_s (m/s/m)	ρ_s (g/cm³)	a_s (dB/m/kHz)	H_s (m)	c_b (m/s)	ρ_b (g/cm³)	a_b (dB/m/kHz)	range (m)
S3 (p)	1500	3.3	1.36	0.10	3.5	1670	2.37	0.39	3100
S3 (u_z)	1519	0.7	1.38	0.04	7.9	1673	2.14	1.75	3093
S4 (p)	1501	4.9	1.51	0.02	3.8	1677	2.29	0.67	3081
S4 (u_z)	1508	3.0	1.39	0.06	5.1	1684	2.20	1.43	3089
S3 (p, u_z)	**1503**	**7.2**	**1.55**	**0.24**	**4.8**	**1672**	**2.31**	**0.66**	**3090**
S4 (p, u_z)	**1505**	**7.7**	**1.48**	**0.10**	**4.1**	**1672**	**2.28**	**0.68**	**3080**

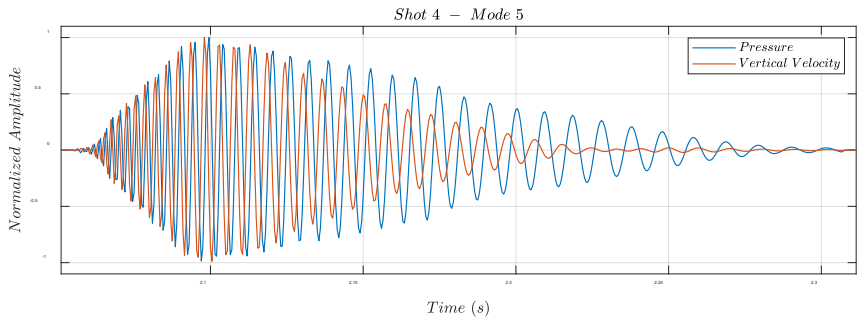

Figure 42. Shot 4's mode 5 waveforms for pressure and vertical velocity after the separation using TW with BPF mask.

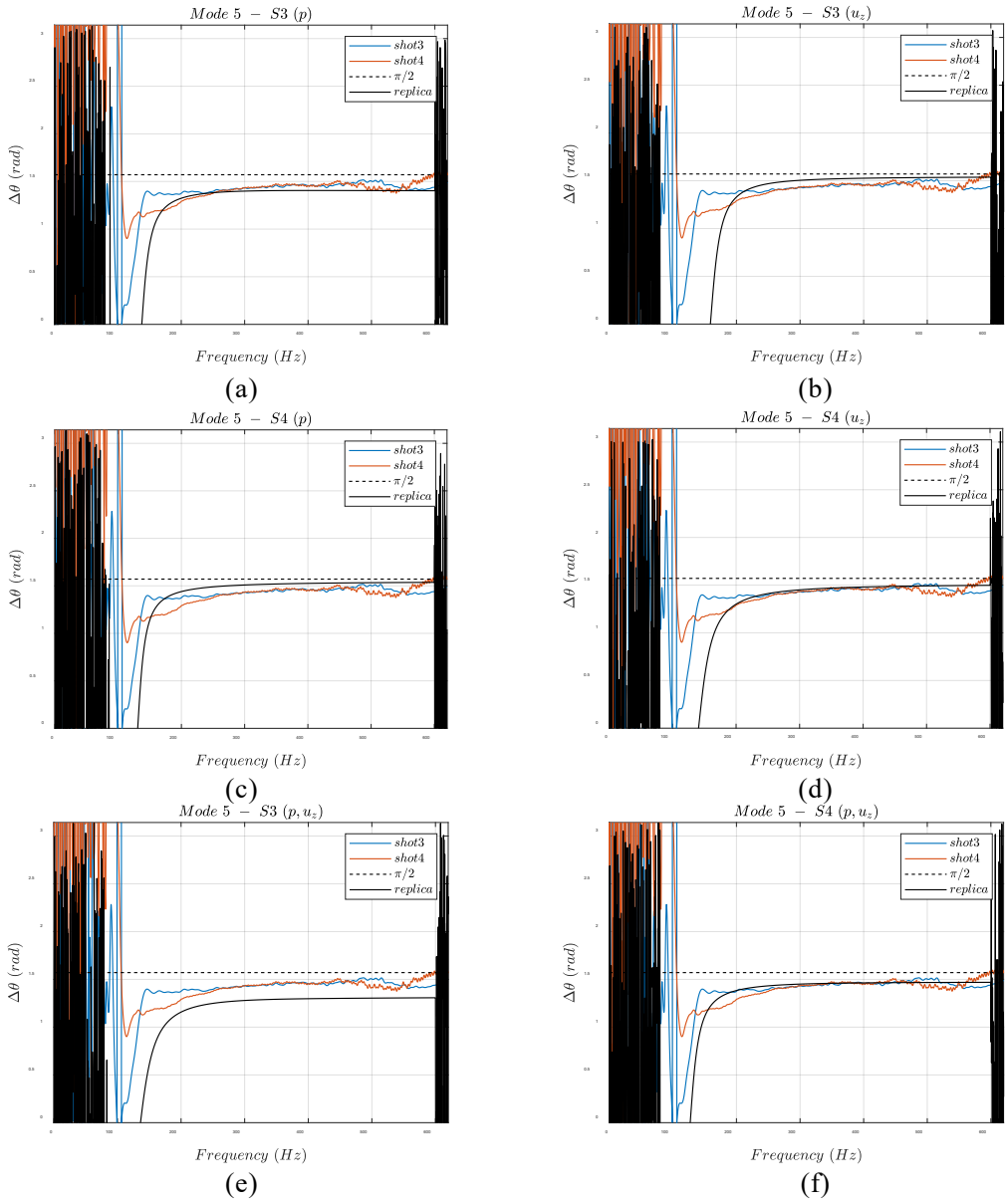

Figure 43. Modal phase difference between pressure and vertical velocity, including shots 3 and 4, and replicas using parameters of Table 4. (a) S3 (p). (b) S3 (u_z). (c) S4 (p). (d) S4 (u_z). (e) S3 (p, u_z). (f) S4 (p, u_z).

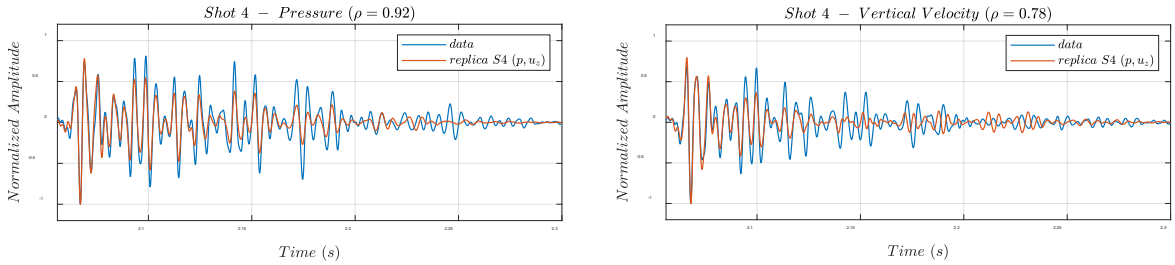

(a) (b)

Figure 44. Comparison of waveforms between data and replica using inverted values S4 (p, u_z). Pressure with correlation coefficient of 0.92 (a). Vertical velocity with correlation coefficient of 0.78 (b).

G. COMPARISON BETWEEN DC AND WAVEFORM MATCHING INVERSIONS

To compare results from both techniques, the waveform matching inverted parameters $S4\ (p, u_z)$ are used to generate synthetic DCs. Figure 45 shows the comparison considering only the pressure signal.

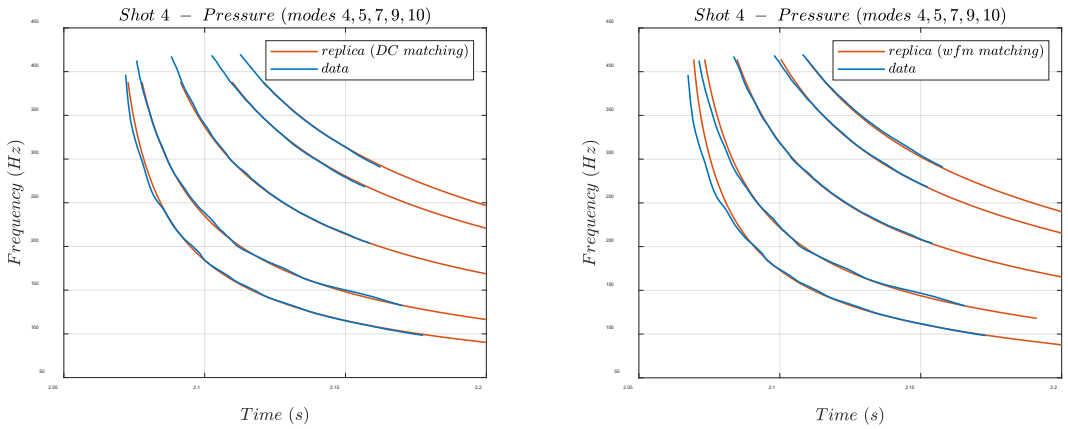

(a) (b)

Figure 45. Comparison between inversion techniques. The DC replica uses DC inversion inverted parameters (a). The DC replica uses waveform matching inverted parameters (b).

The synthetic DCs using waveform matching shown in Figure 45(b) reveals the distortions in data for mode 4 above 200 Hz, mode 5 above 250 Hz, and modes 7 and 9 above 365 Hz. Such distortions are caused by intermodal interference in the warped-

domain, more pronounced within the low order modes at higher frequency components since the modes travel more closely together, as shown in the spectrogram of Figure 40(a). This effect ends up overestimating sediment sound speed in the DC inversion from 1505 to 1577 m/s, for instance. Doing the DC inversion again suppressing those portions of data, Table 5 compares DC inversion without suppression, DC inversion with suppression, and waveform matching. As expected, the results improve, getting closer to the ones estimated by the waveform matching.

Table 5. Comparison of results between DC inversion and waveform matching suppressing parts of the DCs to improve results.

	c_s (m/s)	∇c_s (m/s/m)	ρ_s (g/cm^3)	a_s (dB/m/kHz)	H_s (m)	c_b (m/s)	ρ_b (g/cm^3)	a_b (dB/m/kHz)	range (m)
Shot 4 (DC no suppression)	1577	7.5	1.32	x	6.4	1773	1.60	x	3083
Shot 4 (DC with suppression)	1509	1.3	1.44	x	3.6	1674	1.76	x	3090
S4 (p, u_z) (waveform matching)	1505	7.7	1.48	0.10	4.1	1672	2.28	0.68	3080

H. DISCUSSION

The DC inversion using TW to separate modes is broadly used [2, 13, 15]. One of its advantages is related to the optimization process that requires less parameters to match, since the travel time of normal modes, for example, is not sensitive to the bottom attenuation. On the other hand, small changes in the environmental parameters cause small changes in the DC shapes, which makes the technique susceptible to the distortions caused by the separation of modes, for signal processing reasons and physical reasons, like noise contamination. Aside from that, the tendency is to maximize the DCs energy content, which means to separate the DCs with the longest duration in time as much as possible to optimize results. However, this chapter shows that such distortions can be very subtle. There is no indication in Figure 40(c) of low quality DCs, for example. On the other hand, when the same DCs were put against the waveform matching, the distortions became visible. The suppression of those regions improved results as shown in Table 5 but decreased the energy content of the DCs, making the optimization less sensitive to some

parameters, which affected the estimation of sediment sound speed gradient and range, for instance.

As for the waveform matching technique, the bottom reflectivity and attenuation affect the mode amplitudes in the receiver. Then, an erroneous estimation of one can adversely affect the estimation of the other. Therefore, this chapter shows that a more robust estimation of bottom attenuation is obtained when a vector sensor is applied using the modal phase difference between pressure and vertical velocity. In this chapter, such calculation was used to refine the inverted parameters of Table 4. However, it can be easily incorporated to the cost function of the optimization process.

Additionally, Figure 44(b) shows that it is harder to match the vertical velocity signal compared to the pressure signal, which is shown in Figure 44(a) with a correlation coefficient of 0.92. That can be related to the simplicity of the bottom effective model. However, the correlation coefficient of 0.78 for the vertical velocity was helpful to the simultaneous matching that generated more stable results as shown in Table 4.

The estimated parameters are consistent with the ground truth information about the region being composed by mud, very fine sand, and silt according to the California Seafloor Mapping Program [31].

Finally, the results suggest based on the environment considered and data analysis of this chapter, although waveform matching can be used to improve the DC inversion, when a vector sensor is available for geoacoustic inversion, waveform matching performs better.

I. CONCLUSION

This chapter discussed the value added by using waveform matching as a preliminary step to improve the performance of the DC inversion method. The separation of modes using TW methods causes distortions to the retrieved DCs, for signal processing or physical reasons, like noise contamination. The results showed that waveform matching can be used to check the quality of the DCs retrieved from data and improve results.

Although the waveform matching technique has more parameters to match, like the bottom attenuation coefficient, we show that when a vector sensor is available, waveform matching results can be refined. First, doing the simultaneous matching of pressure and vertical velocity, and second, using the modal phase difference approach. Although in this chapter such approach was used to refine results after the inversion, if KRAKENC is used for the waveform matching, full-field and individual mode predictions can be included, and the modal phase difference between pressure and vertical velocity can be incorporated to the cost function of an optimization process, which narrows down the bottom attenuation calculation, avoiding erroneous estimations within correlated parameters. Overall, this study suggests that when a vector sensor is available for geoacoustic inversion, waveform matching can improve results of the DC inversion technique, but in the environment considered in this chapter, waveform matching is a better option.

THIS PAGE INTENTIONALLY LEFT BLANK

V. CONCLUSIONS

This dissertation is a collection of three peer-reviewed articles: the first one [9] published in the *Journal of Theoretical and Computational Acoustics (*JTCA*)*, the second one [10] under review in the same Journal, and the third one [11] under review in the *24th International Congress on Acoustics (ICA2022)*.

The articles present new approaches for the inversion of geoacoustic parameters using a vector sensor. A lot of attention has been given to this type of sensor by the acoustics community to improve results previously obtained with pressure-only analysis. Besides its important application in target tracking, this dissertation focused on the geoacoustic inversion of environmental parameters, where direction finding is not the main interest. The research was conducted using synthetic predictions and data. Two propagation models were used, the normal mode model KRAKEN and the parabolic equation model RAM, both being modified to include predictions of the vector field. It was also important to use both models for comparison and calibration purposes. Data was collected on the northern shelf of Monterey Bay in 2019, using lightbulb implosions, a reference hydrophone for source signature acquisition and depth estimation, a vector sensor system, and a CTD for SSP measurements. To improve performance, a hybrid optimization approach was adopted using GA and Bayesian optimization, and both propagation models were also changed for parallel processing capabilities. For the inversion, two normal mode features were used, the travel time and modal phase difference, and TW was used for modes separation.

In Chapter II [9], the modal phase difference approach was investigated using synthetic signals, and the technique derived based on a Pekeris waveguide, which is an environmental model with analytic solutions for the pressure field. In this chapter, we first modified the TW process, where a Tukey window was included in the time-domain before the warping operation. Second, a columnwise band-pass filter approach was used in the time-frequency domain. Independent filters were calculated for each column of the STFT matrix for each mode. Both implementations were done to fight the inherent abrupt transitions of the TW process. Next, we showed that the modal phase difference between

pressure and vertical velocity has a much larger span in phase than using the radial velocity, which is the reason why the vertical velocity is better suited for real-world applications. The modal phase difference between pressure and radial velocity tends to be very small, and therefore more susceptible to signal processing artifacts. The technique was evaluated adding white noise before the warping transformation at different SNRs. We showed that loud signals with SNR > 20 dB is necessary for better results, which is perfectly achievable using implosive (e.g., light bulbs) or explosive (e.g., SUS) sources. The technique was also evaluated using a real SSP, which was scaled by a constant factor to evaluate SSP uncertainty, and the results showed low sensitivity to the SSP. Furthermore, if the adiabatic approximation remains valid and normal modes are separated, the technique can be applied in more complicated situations like RD and HI waveguides. The proposed technique has the meaning of the attenuation at the receiver site, not the path-averaged bottom attenuation, making it a possible candidate to shallow-water real-world applications.

In Chapter III [10], we investigated the value added by averaging DCs, using different combinations of channels of a vector sensor. A preliminary analysis was done using synthetic signals. KRAKEN was utilized to compute DCs using group speed and individual mode waveforms, both applying an adiabatic approximation, and RAM was used for full-field predictions. TW was used to separate individual modes. Three combinations of channels were evaluated using KRAKEN individual mode waveforms, and six using RAM. White noise was also included to the RAM full-field predictions at different SNRs. In the synthetic analysis we evaluated (1) the performance of the technique when TW is not used, since KRAKEN provides the modes already separated, (2) the performance using TW with the TRAD and BPF masks, (3) the performance of the different channels combinations, and (4) the impact of signal excess on the results. We showed that the vertical channel offers added value to the pressure-only analysis. A positive net contribution of averaging pressure and vertical velocity DCs reduces distortions, like the ones caused by the reassigned spectrogram and ridge function, which resulted in a modest improvement when the combination was used. We also showed that the BPF mask improved results over the TRAD mask, which suggests, in accordance with Chapter II, that the TRAD mask should not be the first option when TW is applied. Still, a

SNR > 20 dB is desirable for better results. In the case of the data analysis, the results suggest that data from the vertical channel can help to reduce uncertainty in the parameter estimates. However, since each geoacoustic parameter has a different effect on the DC shape, the combination can possibly be beneficial for some parameters, but not for all. It was difficult to exactly quantify the trend using data, due to the limitation of two light bulb implosions.

In Chapter IV [11], a comparison was done between the DC inversion and the waveform matching using the vector sensor data of the previous chapter. The DC inversion was applied using the combination of pressure and vertical velocity, and the modes were separated using TW with BPF mask, which according to chapters II and III is the best option. The waveform matching was applied using pressure and vertical velocity signals individually and simultaneously, which resulted in six sets of inverted parameters. The modal phase difference between pressure and vertical velocity was then used to select the best estimate among the six outcomes. The inversion using DCs overestimated some parameters like sediment sound speed, for instance. The erroneous estimation was identified using waveform matching, which helped to highlight the distortions on the DCs. We then showed that, after the suppression of the portions of DCs with distortions, value was added improving the results of the DC inversion. However, since the suppression decreased the energy content of the DCs, which made the optimization less sensitive to some parameters, it was not possible to obtain results as good as the waveform matching. In summary, the data used in this chapter suggests that when a vector sensor is available for geoacoustic inversion, waveform matching performs better.

Regarding areas for future research, the DC inversion is affected by the DC quality, which is directly connected to the way DCs are retrieved. DC inversion has a great advantage over the waveform matching, since fewer parameters are necessary in the optimization process. However, the DC distortion is a limiting factor, and one should investigate different ways to obtain cleaner DCs. Finally, although the modal phase difference approach was used in this dissertation to refine results of the inversion using waveform matching, one should test the incorporation of the modal phase difference to the optimization process.

THIS PAGE INTENTIONALLY LEFT BLANK

LIST OF REFERENCES

[1] J. Bonnel, A. Thode, D. Wright, and R. Chapman, “Nonlinear time-warping made simple: A step-by-step tutorial on underwater acoustic modal separation with a single hydrophone,” *J. Acoust. Soc. Am. ,* vol. 147, no. 3, pp. 1897–1926, 2020.

[2] J. Bonnel and N. R. Chapman, “Geoacoustic inversion in a dispersive waveguide using warping operators,” vol. 130, no. 2, pp. EL101-EL107, 2011.

[3] N. R. Chapman and E. C. Shang, “Review of Geoacoustic Inversion in Underwater Acoustics,” *J. Theor. Comput. Acoust.,* vol. 29, no. 3, pp. 31–33, 2021.

[4] L. Zheng-Lin and Z. Ren-He, “Geoacoustic Inversion Based on Dispersion Characteristic of Normal Modes in Shallow Water,” *Chinese Physics Letters,* vol. 24, no. 2, pp. 471–474, 2007.

[5] G. R. Potty, J. H. Miller, and J. F. Lynch, “Inversion for sediment geoacoustic properties at the New England Bight,” *J. Acoust. Soc. Am.,* vol. 114, no. 4, pp. 1874–1887, 2003.

[6] J. Zhou, “Normal mode measurements and remote sensing of sea-bottom sound velocity and attenuation in shallow water,” *J. Acoust. Soc. Am.,* vol. 78, no. 3, pp. 1003–1009, 1985.

[7] M. B. Porter, “The KRAKEN normal mode program,” October 1997. [Online]. Available: https://oalib-acoustics.org/AcousticsToolbox/manual/kraken.html. [Accessed November 2020].

[8] M. D. Collins, “User’s Guide for RAM Versions 1.0 and 1.0p,” Naval Research Laboratory.

[9] A. Guarino, K. B. Smith and O. A. Godin, “Bottom attenuation coefficient inversion based on modal phase difference between pressure and vertical velocity from a single vector sensor,” *J. Theor. Comput. Acoust.,* pp. 1–16, 2021, https://doi.org/10.1142/S2591728521500080.

[10] A. L. Guarino, K. B. Smith, K. Gemba and O. A. Godin, “Geoacoustic inversion with a single vector sensor and multichannel dispersion,” *J. Theor. Comp. Acoust.,* pp. 1–18, 2022, “Submitted for review.”

[11] A. L. Guarino, K. B. Smith, K. Gemba, and O. A. Godin, “Geoacoustic inversion using waveform matching as a preliminary step in dispersion curve analysis to assess bottom attenuation from a single vector sensor,” in *24th International Congress on Acoustics*, Gyeongju, Korea, 2022, “Submitted for review.”

[12] K. Smith, J. Hermand and A. Leijen, “Estimation of Sediment Attenuation from Measurements of the Acoustic Vector Field,” *Theoretical and Computational Acoustics, University of Crete and Foundation for Research and Technology, Hellas,* pp. 31–38, 2007.

[13] R. Duan, N. R. Chapman, K. Yang, and Y. Ma, "Sequential inversion of modal data for sound attenuation in sediment at the New Jersey Shelf," *J. Acoust. Soc. Am.,* vol. 139, no. 1, pp. 70–84, 2016.

[14] J. Bonnel, Y. Lin, D. Eleftherakis, J. A. Goff, S. Dosso, R. Chapman, J. H. Miller, and G. R. Potty, "Geoacoustic inversion on the New England Mud Patch using warping and dispersion curves of high-order modes," *J. Acoustic. Soc. Am.,* vol. 143, no. 5, pp. EL405-EL411, 2018.

[15] O. A. Godin, B. G. Katsnelson, and T. W. Tan, "Normal mode dispersion and time warping in the coastal ocean," *J. Acoust. Soc. Am. ,* vol. 146, no. 3, pp. 205–211, 2019.

[16] A. Tolstoy, N. R. Chapman, and G. Brooke, "Workshop '97: Benchmarking for geoacoustic inversion in shallow water," *Journal of Computational Acoustics,* vol. 6, no. 1–2, pp. 1–28, 1998.

[17] R. G. Baraniuk and D. L. Jones, "Unitary equivalence: A new twist on signal processing," *IEEE,* October 1995.

[18] J. Bonnel, S. Dosso, and R. Chapman, "Bayesian geoacoustic inversion of single hydrophone light bulb data using warping dispersion analysis," *J. Acoust. Soc. Am.* vol. 134, no. 1, pp. 120–130, 2013.

[19] G. A. Warner, S. E. Dosso, J. Dettmer, and D. E. Hannay, "Bayesian environmental inversion of airgun modal dispersion using a single hydrophone in the Chukchi Sea," *J. Acoust. Soc. Am.* vol. 137, no. 6, p. 2361–2362, 2015.

[20] T. W. Tan and O. A. Godin, "Characterizing the seabed in the Straits of Florida by using acoustic noise interferometry and time warping," *J. Acoust. Soc. Am.,* vol. 146, no. 4, pp. 2321–2334, 2019.

[21] J. Zeng, N. R. Chapman, and J. Bonnel, "Inversion of seabed attenuation using time-warping of close range data," *J. Acoust. Soc. Am.,* November 2013.

[22] P. H. Dahl and D. R. Dall'Osto, "Vector acoustic analysis of time-separated modal arrivals from explosive sound sources during the 2017 seabed characterization experiment," *J. Oceanic Eng.,* vol. 45, no. 1, 2020.

[23] J. Shi, S. E. Dosso, D. Sun, and Q. Liu, "Geoacoustic inversion of the acoustic -pressure vertical phase gradient from a single vector sensor," *J. Acoust. Soc. Am.,* November 2019.

[24] P. H. Dahl and D. R. Dall'Osto, "Estimation of seabed properties and range from vector acoustic observations of underwater ship noise," *J. Acoust. Soc. Am.,* vol. 147(4), pp. EL345-EL350, 2020.

[25] L. M. Brekhovskikh and O. A. Godin, Acoustics of layered media 2: point sources and bounded beams, 2nd ed., Berlin, Germany: Springer, 1999, pp. 244–282.

[26] R. Duan, N. R. Chapman, K. Yang, and Y. Ma, “Sequential inversion of modal data for sound attenuation in sediment at the New Jersey Shelf,” *J. Acoust. Soc. Am.,* vol. 139, no. 1, pp. 70–84, 2016.

[27] P. Santos, O. Rodríguez, P. Felisberto, and S. Jesus, “Seabed geoacoustic characterization with a vector sensor array,” *J. Acoust. Soc. Am.,* vol. 128, no. 5, p. 2652–2663, 2010.

[28] O. Rodríguez, P. Felisberto, E. Ey, J. Schneiderwind, and S. Jesus, “Vector sensor geoacoustic estimation with standard arrays, ECUA 2012 11th European Conference on Underwater Acoustics, Edinburgh, Scotland,” in *J. Acoust. Soc. Am., vol. 17, pp. 1–10*, 2012.

[29] D. R. Dall’Osto, J. W. Choi, and P. H. Dahl, “Measurement of acoustic particle motion in shallow water and its application to geoacoustic inversion,” *J. Acoust. Soc. Am.,* vol. 139, no. 1, pp. 311–319, 2016.

[30] S. E. Turner, “Underwater implosion of glass spheres,” *J. Acoust. Soc. Am.,* vol. 121, no. 2, pp. 844–852, 2007.

[31] P. Dartnell, K. Maier, M. Erdey, B. Dieter, N. Golden, S. Johnson, S. Hartwell, et al., “Monterey Canyon and Vicinity, California: U.S. Geological Survey Open-File Report 2016–1072, 48 p., sheet 10, scale 1:24,000,” California State Waters Map Series, 2016. [Online]. Available: http://dx.doi.org/10.3133/ofr20161072.

[32] F. B. Jensen, W. A. Kuperman, M. B. Porter, and H. Schmidt, *Computational Ocean Acoustics,* New York, NY, USA: Springer, 2011.

[33] T. A. El-Mihoub, A. A. Hopgood, L. Nolle, and A. Battersby, “Hybrid genetic algorithms: A review,” *Engineering Letters,* vol. 13, no. 2, pp. 1–15, 2006.

[34] “MathWorks Support: ga (Find minimum of function using genetic algorithm),” [Online]. Available: https://www.mathworks.com/help/gads/ga.html. [Accessed February 2022].

[35] “MathWorks Support: bayesopt (Select optimal machine learning hyperparameters using Bayesian optimization),” [Online]. Available: https://www.mathworks.com/help/stats/bayesopt.html. [Accessed February 2022].

[36] “MathWorks Support: predictObjective (Predict objective function at a set of points),” [Online]. Available: https://www.mathworks.com/help/stats/bayesianoptimization.predictobjective.html. [Accessed February 2022].

[37] K. Gemba, H. J. Vazquez, J. Fialkowski, G. F. Edelmann, M. A. Dzieciuch, and W. S. Hodgkiss, “A performance comparison between m-sequences and linear frequency-modulated sweeps for the estimation of travel-time with a moving source,” *J. Acoust. Soc. Am.,* vol. 150, no. 4, p. 2613–2623, 2021.

[38] C. Reeves, “Genetic algorithms and neighbourhood search. In: Fogarty T. C. (eds) Evolutionary computing. AISB EC 1994. Lecture Notes in Computer Science, vol 865. Springer, Berlin, Heidelberg.,” 1994. [Online]. Available: https://doi.org/10.1007/3-540-58483-8_10.

INITIAL DISTRIBUTION LIST

1. Defense Technical Information Center
   Ft. Belvoir, Virginia

2. Dudley Knox Library
   Naval Postgraduate School
   Monterey, California